Heralding entangled optical photons from a microwave quantum processor

(article starts on next page)

Heralding entangled optical photons from a microwave quantum processor

Trond Hjerpekjøn Haug [*], Anton Frisk Kockum, and Raphaël Van Laer [†]

Department of Microtechnology and Nanoscience, Chalmers University of Technology,
SE-412 96 Gothenburg, Sweden

Exploiting the strengths of different quantum hardware components may increase the capabilities of emerging quantum processors. Here we propose and analyze a quantum architecture that leverages the nonlocal connectivity of optics, along with the exquisite quantum control offered by superconducting microwave circuits, to produce entangled optical resource states. In contrast to previous proposals on optically distributing entanglement between superconducting microwave processors, we use squeezing between microwaves and optics to produce microwave-optical Bell pairs in a dual-rail encoding from a single microwave quantum processor. Moreover, the microwave quantum processor allows us to deterministically entangle microwave-optical Bell pairs into larger cluster states, from which entangled optical photons can be extracted through microwave measurements. Our scheme paves the way for small microwave quantum processors to create heralded entangled optical resource states for optical quantum computation, communication, and sensing using imperfect microwave-optics transducers. We expect that improved isolation of the superconducting processor from stray optical fields will allow the scheme to be demonstrated with currently available hardware.

I. INTRODUCTION

Entanglement is a central resource for quantum computation, communication, and sensing [1]. For quantum technology platforms such as superconducting microwave circuits [2,3], continuous-variable optics [4,5], and trapped ions [6–8], controlled generation of entanglement is now a routine task, while for discrete-variable optics it remains a daunting challenge [9]. Optical entanglement can be produced probabilistically through fusion measurements [10–12] on single optical photons heralded from second-order [13–15] and third-order [16–18] spontaneous biphoton emission. Alternatively, optical quantum emitters can entangle optical photons deterministically via spin-photon interactions [19–25]. A less-explored path to produce entanglement between single optical photons is to prepare the entangled state in a mature platform with a strong quantum nonlinearity—such as superconducting microwave circuits—and then transduce the state to optics. This approach places strict performance

requirements on microwave-optics transducers [26,27]. Despite rapid progress in recent years, current transduction platforms cannot yet directly convert quantum states between microwaves and optics [28–33].

In this work, we present a scheme for producing entangled optical states, called "resource states," using microwave-optics transducers. Each qubit in the resource state is encoded as a dual-rail erasure qubit—the preferred code for discrete-variable optical quantum technologies. Our scheme goes beyond previous proposals for heralding single microwave-optical photon pairs [34,35]: we propose a full architecture for a microwave quantum processor to produce multiqubit optical resource states. The architecture is designed to meet the requirements set by fault-tolerant optical quantum technologies such as all-optical quantum repeaters [36] and fusion-based quantum computers [12]. We present the fundamental building block in the architecture, which heralds microwave-optical Bell pairs with spectrally pure optical photons. We show how such microwave-optical Bell pairs can be naturally interpreted as the vertices of microwave-optical graph states constructed with the superconducting processor, and how measurements of the superconducting qubits produce an all-optical graph state identical to the hybrid microwave-optical graph state. Finally, we find a set of performance parameters for each component in our architecture where all-optical resource states can be efficiently constructed with error rates near the threshold for fault-tolerant fusion-based quantum computation (FBQC).

---

[*]Contact author: trond.haug@chalmers.se
[†]Contact author: raphael.van.laer@chalmers.se

We describe in detail how hardware imperfections translate into qubit errors that must be handled by the quantum error-correcting code, and we identify optical loss and thermal noise in the transducer as the main areas of improvement for future experimental implementations.

The scheme presented enables the creation of a modular, fault-tolerant quantum computer with superconducting processors as resource-state generators (RSGs) seeding an optical processor that implements logic and error correction [37]. It takes advantage of the recent development of dual-rail architectures for superconducting quantum processors that aims to make such processors capable of fault-tolerant quantum computing [38–40]. However, the construction of a single RSG is much simpler than that of a fault-tolerant superconducting processor. RSGs capable of producing resource states of n optical dual-rail qubits require only $\sim n/p$ physical superconducting dual-rail qubits, where p is the microwave-optical heralding probability per clock cycle. With the proposed architecture, we simulate the preparation of a microwave-optical Bell state and find that $p \lesssim 20\%$ for practical applications. Therefore, integration of approximately 100 dual-rail qubits on a single chip would be sufficient to build RSGs capable of producing optical resource states with $n \sim 20$ qubits for fault-tolerant fusion-based quantum computation [41,42]. This proposal provides optical quantum processors with the main element lacking in their architecture: a fast source of low-overhead optical entanglement. To the best of our knowledge, it is the first to propose and study microwave quantum processors as resource-state generators, i.e., "entanglement factories" for optical quantum technologies. The well-known schemes for connecting microwave qubits through optically mediated entanglement [43,44] use only limited optical technology. This work initiates a wider research landscape where quantum processing can take place in both the optical domain and the microwave domain.

This modular approach to building a fault-tolerant quantum processor has several potential advantages compared with building a full-size processor exclusively from superconducting qubits. First, a single RSG needs fewer physical qubits than fault-tolerant microwave processors, thus bypassing the need to scale such processors beyond the current state of the art. Second, no logical information is stored on the microwave processor, which can be corrupted by ionizing radiation or high-energy impacts [45,46]. Such events would temporarily halt the production of resource states from an RSG, but this could be compensated by one routing resource states from a different RSG with minimal overhead. Third, the traveling optical photons in the resource states can be used to implement high-threshold surface codes concatenated with efficient low-density parity-check (LDPC) codes that require nonlocal connections [47,48]. We can make further use of the

nonlocal connections to implement an active-volume logical architecture [49]. This reduces the resource cost for a quantum computation by minimizing the number of idling qubits during a computation, with potentially orders-of-magnitude gains for large computations. Fourth, the logical processing is done entirely through destructive measurements, which implies that qubit leakage (e.g., transmons excited to the state $|f\rangle$) does not cause errors that stabilizer fault tolerance is not designed to handle [50,51].

In the near term, the use of imperfect microwave-optics transducers requires a mixed heralded-deterministic scheme (Fig. 1) to generate the optical entanglement from heralded microwave-optical qubit pairs and deterministic microwave gates. If microwave-optics transducers continue to improve on their current steep path [28–33,52], the optical entanglement can eventually be generated deterministically through direct transduction of the entangled microwave photons. In contrast to purely microwave-frequency approaches to exploit LDPC codes [53] and hardware-efficient resource states using tailored delay lines [54], optical photons are ideal for the nonlocal connectivity needed in LDPC codes given their low noise, loss, and crosstalk in widely available optical fiber delay lines even at room temperature. This proposal takes a step forward on the overarching question of how the strengths of optical and microwave photons as quantum information carriers can be combined and harnessed optimally.

This paper is organized as follows. We begin by introducing hardware capable of implementing our proposed scheme in Sec. II. In Sec. III, we describe the protocol for producing optical resource states at the fundamental level in the absence of hardware imperfections. We then look at the performance of the protocol when accounting for errors and hardware imperfections in Sec. IV. Specifically, we discuss hardware-independent, intrinsic errors related to optomechanical squeezing in Sec. IV A and hardware-dependent errors in Sec. IV B. In Sec. IV C, we show that the qubit errors form a hierarchy, with relatively benign erasure errors as the dominant error type. Section IV D gives a brief overview of the expected effects of optically induced quasiparticle poisoning of the superconducting qubits in our scheme and how this can be mitigated. Finally, we show how the hardware overhead of our scheme compares with that of currently pursued schemes for scaling up quantum processors that use only optics (Sec. V A) or only stationary microwave qubits (Sec. V B).

II. HARDWARE IMPLEMENTATION

Our proposal is based on a dual-rail encoding of qubits in both the microwave domain and the optical domain. On the optical side, the dual-rail qubit is a flying optical photon in one of two identical waveguides, as illustrated in Fig. 2(a). Such photons can be stored in optical fiber
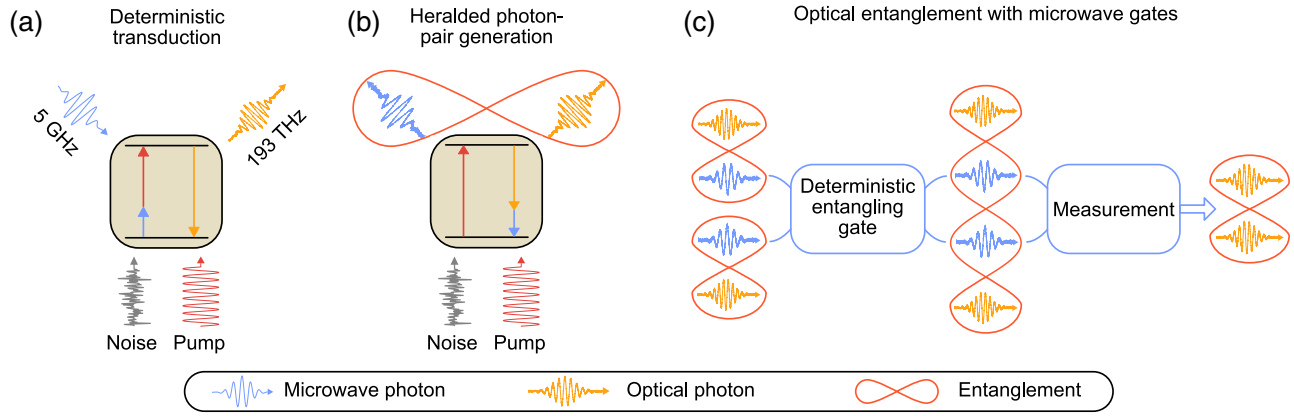
FIG. 1. Generation of optical entanglement through microwave-optics photon-pair generation and deterministic microwave gates. (a) High-performance microwave-optics transducers could convert incoming microwave photons to optical photons using an optical pump to bridge the energy gap. Trade-offs between added noise and efficiency prevent today's transducers from converting quantum states deterministically. (b) Even imperfect microwave-optics transducers can be operated as high-fidelity probabilistic photon-pair generators. In this work, the presence of a microwave photon—detected through a microwave parity check—heralds an entangled microwave-optical photon pair. (c) We propose leveraging deterministic microwave gates on several such pairs to generate optical entanglement. The entanglement structure of the full microwave-optical quantum state can be transferred to an all-optical quantum state by measurements in the microwave domain. This allows deterministic entanglement swapping from microwave-optical states to all-optical states.

with transmission loss rates of less than 0.2 dB/km—or 1% per microsecond—at telecom wavelengths. On the microwave-frequency side, a dual-rail qubit is formed by a single excitation trapped in one of two stationary modes of microwave cavities [38], electromechanical resonators [55–57], or qubits such as the transmon [39,40,58]. Regardless of the nature of the microwave dual-rail component, deterministic microwave gates exploiting Josephson junctions generate the microwave entanglement to be transferred to optics. Both cavities and qubits have attractive properties for building the microwave dual-rail component. First, superconducting cavities currently have intrinsic relaxation times of approximately 1 ms and dephasing times of approximately 10 ms [38]. Second, electromechanical resonators are developing as an alternative to microwave cavities. They may eventually provide advantages in lifetime, crosstalk, and compactness [55–57,59], yet are currently less mature. Third, transmons typically decohere faster than microwave cavities, with common relaxation and dephasing times of $\lesssim 100\,\mu s$. They are a widely adopted and mature technology and have proven to be manufacturable on the scale needed for a single RSG [60–62]. The dephasing time for a dual-rail qubit based on flux-tunable transmons can be made comparable to that of cavities by a resonant coupling between the transmons [39,40,63]. The resulting splitting of the two hybridized transmon modes is first-order insensitive to flux noise in the individual transmons, thus removing the largest source of dephasing for flux-tunable transmons, while retaining their extraordinary versatility and fast two-qubit gates. For concreteness, we choose the

transmon-based implementation of the microwave dual-rail component in the following analysis.

A microwave dual-rail qubit is sketched in Fig. 2(b), with two transmons serving as the rails for the dual-rail qubit and a coupler to control the interaction between the rails. The resulting logical subspace and leakage states are illustrated in Fig. 2(c). The computational states of the microwave dual-rail qubit are the symmetric and antisymmetric single-excitation states. A Bloch-sphere representation of the dual-rail qubits is shown in Fig. 2(d). We form a hybrid qubit by combining the microwave and optical dual-rail qubits. We introduce the hybrid-qubit picture in the context of resource-state generation in Sec. III.

The dual-rail qubit can be naturally integrated in large-scale superconducting quantum processors that use a square-grid layout [60,64]. In Fig. 3, we show how we define dual-rail qubits on a square grid of transmon qubits in such a way that each dual-rail qubit in the bulk has six nearest neighbors. To turn the superconducting processor into an RSG, we attach a microwave-to-optics transducer to each transmon in each dual-rail qubit. We refer to a single dual-rail qubit with transducers as a "block." The inset in Fig. 3 shows the circuit diagram of a single block. Each block initializes a dual-rail qubit by combining probabilistic microwave-optical spontaneous down-conversion with deterministic microwave gates. The optical photons are immediately routed to an external optical network through optical fiber. Although our scheme is compatible with any device capable of entangling optical and microwave photons [65], we base the analysis on piezo-optomechanical transducers [28–30,33,66] for
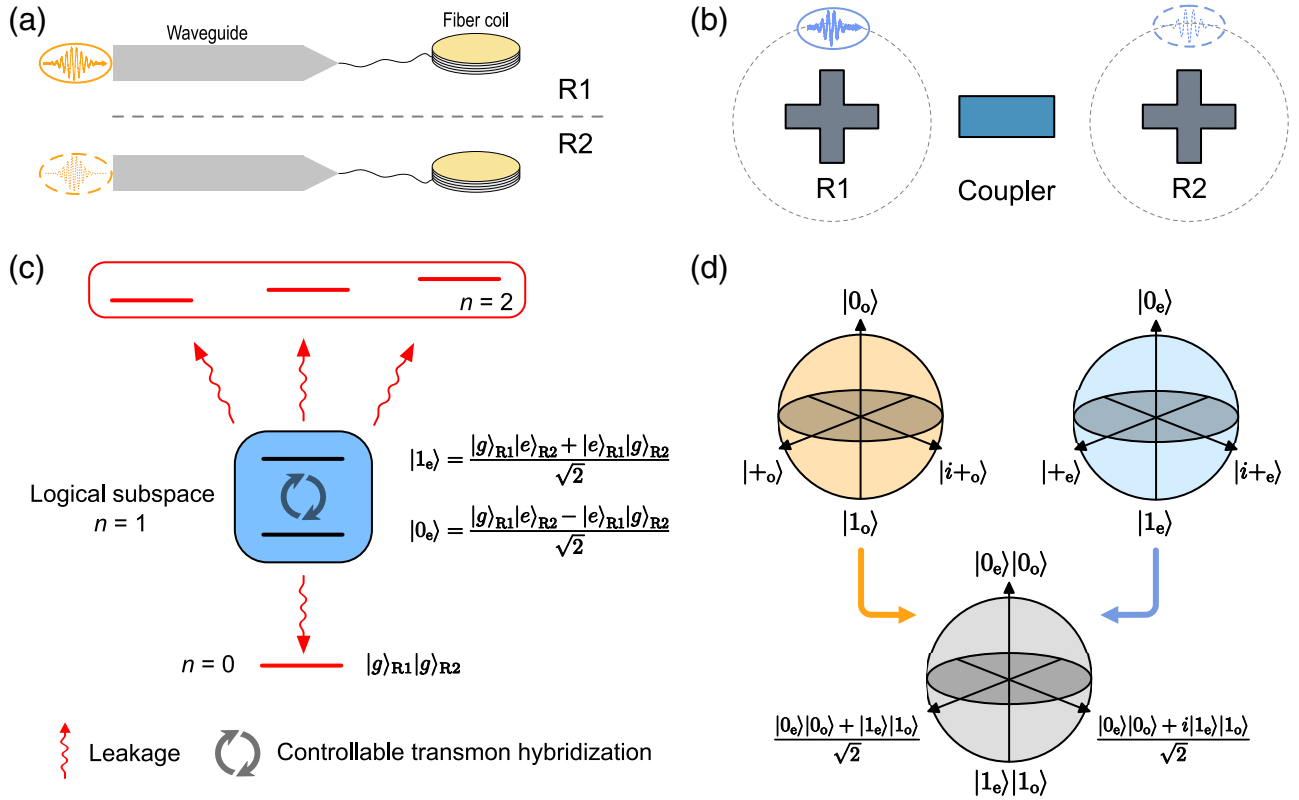
FIG. 2. Dual-rail qubit implemented with optics and transmons. (a) An optical dual-rail qubit consists of a single optical photon in one of two modes, here represented with two physically separated optical waveguides. The waveguides can be interfaced with optical fiber, where photons can be stored before they are measured. "R1" denotes the first rail of the dual-rail qubit and "R2" denotes the second rail. (b) Example implementation of a microwave dual-rail qubit with transmon qubits (crosses) and a coupling element to control the interaction between them. A single microwave photon is stored in the combined system of the two transmons. When we measure the state of each transmon separately, we will find the photon either in R1 or in R2. (c) Energy diagram of the dual-rail qubit in (b), with the dual-rail logical subspace highlighted in dark blue and leakage states highlighted in red. The number of microwave photons is indicated by n for each state. Two hybridized transmons form a two-level system with a controllable gap between the symmetric and antisymmetric single-excitation states, which we use to define the computational basis states of the dual-rail qubit. Photon annihilation and creation bring the system outside the logical subspace, which can be detected with a parity measurement. (d) Bloch-sphere representation of the logical subspace of the dual-rail qubit. The optical and microwave dual-rail qubits can be combined to form a single, hybrid qubit. All hybrid-qubit states apart from the Pauli-Z eigenstates are entangled. The hybrid-qubit picture of entangled microwave and optical qubits is useful when one is constructing resource states, as explained in Sec. III.

concreteness. These transducers support high entangling rates, while dissipating little energy [28,33].

The piezo-optomechanical transducer couples an optical resonator to the transmon via mechanical motion. The frequency dependence of the optical resonator on mechanical motion introduces a three-wave-mixing nonlinearity that couples near-infrared optical modes ($\sim$193 THz) to high-frequency mechanical modes ($\sim$5 GHz). Without loss of generality, we focus on periodically patterned structures in silicon called "optomechanical crystals" (OMCs) [30,31,33] to realize the optomechanical component. A strongly piezoelectric material such as lithium niobate is then used to coherently swap excitations between mechanical mode and the transmon. An optical pump laser incident on the optical cavity bridges the energy

gap between microwaves and optics and increases the optomechanical interaction.

Setting the optical pump frequency ω_L blue-detuned by the mechanical frequency ω_m from the cavity frequency ω_o, we can realize a Hamiltonian that in the rotating frame of the laser takes the form $\hat{H} = \hat{H}_0 + \hat{H}_{int}$ [27,29], with

$$\hat{H}_0 = \frac{1}{2}\hbar\omega_q(t)\hat{\sigma}^z + \hbar\omega_m\hat{b}^\dagger\hat{b} - \hbar\Delta\hat{c}^\dagger\hat{c}, \qquad (1)$$

$$\hat{H}_{int} = \hbar g_{qm}\left(\hat{\sigma}^+\hat{b} + \hat{\sigma}^-\hat{b}^\dagger\right) + \hbar G(t)\left(\hat{b}^\dagger\hat{c}^\dagger + \hat{b}\hat{c}\right), \quad (2)$$

where $\Delta = \omega_L - \omega_o = \omega_m$ is the laser detuning, $\hat{\sigma}^z = |e\rangle\langle e| - |g\rangle\langle g|$ is the transmon's Pauli-Z matrix, $\hat{\sigma}^+$ ($\hat{\sigma}^-$) is the transmon raising (lowering) operator, $\hat{b}^\dagger$ ($\hat{b}$) is the
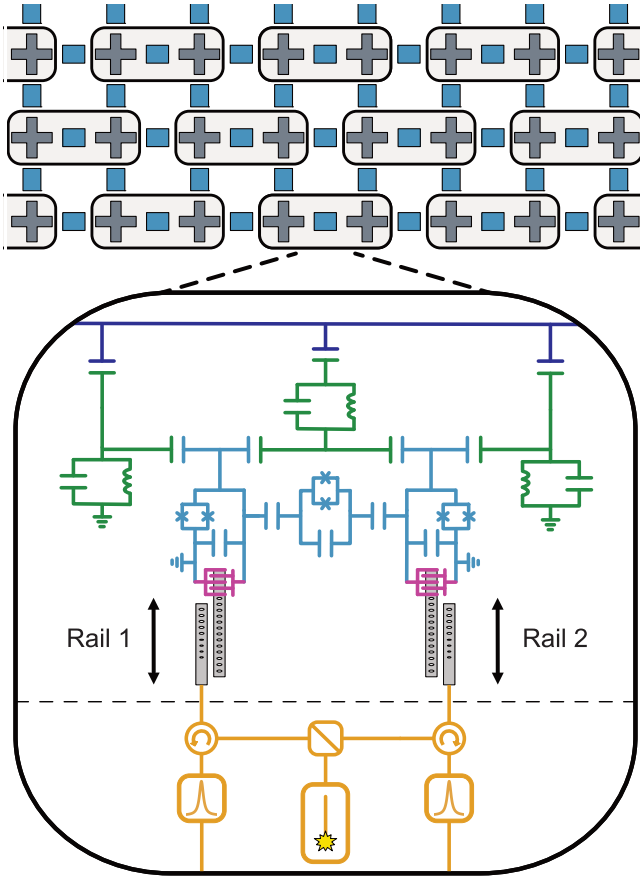
FIG. 3. Overview of the proposed architecture for generating resource states. A superconducting quantum processor [60,61] is divided into dual-rail blocks. Each block contains two superconducting qubits and a tunable coupler (light blue). Tunable couplers also connect qubits belonging to different blocks. To each superconducting qubit we attach electrodes (purple) leading to the piezoelectric region of the microwave-optics transducer. Microwave resonators (green) are used for parity checks and readout of the superconducting qubits through a readout line (deep blue). The dashed line separates the on-chip components from the off-chip optical circuitry (orange), which consists of a pump laser (yellow star), a 50:50 beam splitter, circulators, and pump filters. The pump laser beam is split on the beam splitter, and goes through a circulator into a single-side mirrored optical waveguide evanescently coupled to the piezo-optomechanical transducer (both gray). Optical photons leaving the transducer are directed away from the chip through an optical grating coupler (not shown) and a circulator. The pump is filtered out with the use of, for example, a Fabry-Perot optical filter, producing an optical dual-rail qubit.

creation (annihilation) operator for the mechanical mode, and $\hat{c}^\dagger$ ($\hat{c}$) is the creation (annihilation) operator for the optical mode. The transmon has a flux-tunable frequency $\omega_q(t)$ and couples to the mechanical mode with coupling rate g_{qm}. Thus, the transmon can be brought in and out of resonance with the mechanical mode to control the resonant swapping interactions. The optomechanical coupling

$G(t) = g_{OM}\sqrt{n_c(t)}$ is given by the single-photon optomechanical coupling rate g_{OM} and the intracavity pump photon number n_c.

Previous proposals for heralding microwave-optical Bell pairs [34,35] use a static, resonant coupling between a transducer and a superconducting resonator strongly coupled to a microwave waveguide. However, this configuration does not produce spectrally pure photons when the electrical and mechanical modes are strongly coupled, nor does it implement the multiphoton noise filtering that we propose in Sec. IV. Therefore, the proposed architecture in Fig. 3, which allows a controllable electromechanical swap, is essential for the performance of an RSG.

III. PROTOCOL

We now explain how our architecture heralds microwave-optical Bell pairs and entangles them into graph states. Our protocol runs on a clock cycle, which we refer to as an "RSG cycle." Each block in our architecture executes the same set of instructions every RSG cycle. Figure 4 shows the order of the steps that have to be executed. The RSG cycle time sets the rate at which resource states can be generated from a single superconducting processor. By building several copies of a single RSG, the total resource-state generation rate can be increased without increasing the complexity of control of a single RSG. With fusion-based quantum computing, the size of the resource state remains the same for an arbitrarily large computation—scaling simply becomes a question of how fast we can produce the resource states and how many RSGs we can afford to build. In principle, the resource state can consist of just four optical qubits [12], but bigger resource states tolerate more errors and are therefore desirable [42].

The first step of an RSG cycle is an active reset [67] on all transmons to force them to the ground state. The transmons are detuned away from the mechanical mode of the transducer to which they are coupled so that the electrical and mechanical modes are not yet hybridized, thus ensuring that the photons produced in the optomechanical down-conversion are spectrally pure. A single laser pulse then pumps the two transducers in each dual-rail qubit simultaneously and with equal intensity. In the idealized system, the optomechanical interaction produces the two-mode squeezed vacuum state

$$|\psi\rangle = \sqrt{1 - |\lambda|^2} \sum_{n=0}^{\infty} \lambda^n |n_m\rangle |n_o\rangle \qquad (3)$$

in each transducer, where λ is a squeezing parameter that quantifies the amount of optomechanical spontaneous down-conversion [68] and $|n_m\rangle$ ($|n_o\rangle$) is the nth Fock state of the mechanical (optical) mode. Because the optical cavity is strongly coupled to the external waveguide,
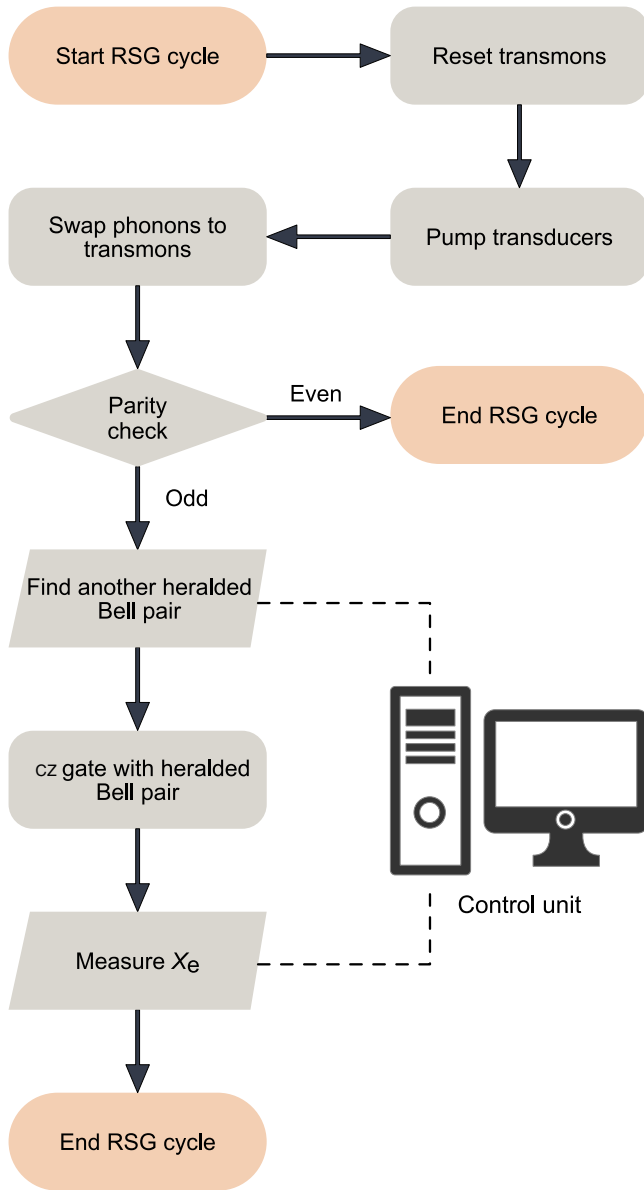
FIG. 4. Process flow in a single RSG cycle. Each block (Fig. 3) undergoes the same set of instructions to herald microwave-optical Bell pairs and entangle them in a graph state. Entangled optical qubits are extracted from the graph state by the measurement of X_e in each block. Oval shapes represent a start or end of a cycle, rectangular shapes represent a step to be executed, diamond shapes represent decisions, and parallelograms represent processes where classical information is either an input or an output.

the optical mode entangled with the mechanics is a traveling wave packet. For an open transducer system coupling to the environment, the state is represented by a density matrix $\hat{\rho}$ and the squeezing is given by the time integral of the optomechanical scattering rate $\Gamma_{OM} = 4|G(t)|^2/\kappa$, with κ the optical linewidth [68]. We return to the treatment of

the open system in Sec. IV. Details on the optomechanical squeezing are provided in Appendix A.

The optical pump pulse prepares each transducer in the state $|\psi\rangle$. Next, the transmons are brought into resonance with the mechanical modes of their respective piezo-optomechanical transducer to swap the phonon to a photon in the transmon. The transmon frequency is tuned by more than g_{qm} in a time shorter than $1/g_{qm}$ so that the swap has high fidelity. This requirement is satisfied with current transmon qubits given $g_{qm}/2\pi \lesssim 10$ MHz [31,56,66,69]. The tunable coupler is set so that the transmons in the rails of the dual-rail qubit do not interact during the swap operation [70,71]. Once the swap is complete, the coupler can be used to turn the interaction between the transmons back on so that the logical qubit subspace is protected from dephasing in the individual transmons [40,63].

The protocol proceeds with a parity check on the dual-rail microwave qubit. Several parity-check protocols apply to our scheme. For example, we can read out the state of a resonator that is symmetrically coupled to the two rail transmons [72–74], as shown in Fig. 3. An odd outcome of the parity check heralds the excitation of one of the two rail transmons, but does not reveal which transmon has been excited, and reveals only that the dual-rail qubit is now inside the logical subspace [Fig. 2(b)]. Each microwave photon is accompanied by an optical photon having left the same transducer before the phonon-photon swap. Therefore, the result of the parity check is that the combined state of the two transmons and the two optical waveguides is projected onto the state

$$|\Psi^+\rangle = (|g0\rangle_{R1}|e1\rangle_{R2} + |e1\rangle_{R1}|g0\rangle_{R2})/\sqrt{2}, \quad (4)$$

where we take the two optical drives to be in phase at their respective OMCs. Here $|g0\rangle$ ($|e1\rangle$) is the state with the transmon in the ground (excited) state and no (one) optical photon in the attached optical waveguide. Crucially, events where no excitation is produced by the pump in either transducer lead to an even outcome in the parity check, as will events where both transmons are excited.

The heralded state $|\Psi^+\rangle$ is a Bell state of an optical dual-rail qubit and a microwave dual-rail qubit. Using the encoding (Fig. 2)

$$|0_e\rangle = (|g\rangle_{R1}|e\rangle_{R2} - |e\rangle_{R1}|g\rangle_{R2})/\sqrt{2}, \quad (5a)$$

$$|1_e\rangle = (|g\rangle_{R1}|e\rangle_{R2} + |e\rangle_{R1}|g\rangle_{R2})/\sqrt{2}, \quad (5b)$$

$$|0_o\rangle = (|0\rangle_{R1}|1\rangle_{R2} - |1\rangle_{R1}|0\rangle_{R2})/\sqrt{2}, \quad (5c)$$

$$|1_o\rangle = (|0\rangle_{R1}|1\rangle_{R2} + |1\rangle_{R1}|0\rangle_{R2})/\sqrt{2}, \quad (5d)$$

one can verify that

$$|\Psi^+\rangle = (|0_e\rangle|0_o\rangle + |1_e\rangle|1_o\rangle)/\sqrt{2}. \quad (6)$$
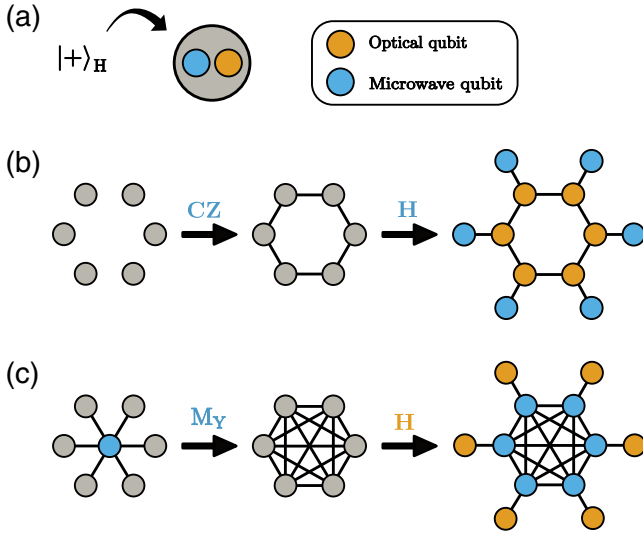
FIG. 5. Generation of microwave-optical resource states. (a) The output from a single block is two entangled dual-rail qubits, which define a single hybrid qubit in the state $|+\rangle_{\mathrm{H}}$. (b) To make a six-ring resource state, we prepare six hybrid qubits (gray) and apply CZ gates between the microwave dual-rail qubits from each logical qubit. This produces a six-ring resource state. A Hadamard gate (H) applied to all microwave qubits in the resource state pushes them out of their logical vertices. (c) A repeater graph useful for quantum communication can also be efficiently constructed with microwave CZ gates and measurements. Here a measurement of the central microwave qubit in the Y basis performs a local complementation of the graph, and a Hadamard gate applied to all optical qubits pushes the optical qubits out of the hybrid vertices.

The state $|\Psi^+\rangle$ can be viewed as a single qubit that has been redundantly encoded in both a microwave qubit and optical qubit. Specifically, we define $|\Psi^+\rangle \equiv |+\rangle_{\mathrm{H}}$ and treat the microwave-optical Bell pair as a single qubit prepared in the $+1$ eigenstate of the operator $\hat{X}_{\mathrm{H}} = \hat{X}_{\mathrm{e}}\hat{X}_{\mathrm{o}}$. The operator $\hat{Z}_{\mathrm{H}}$ has two equivalent representations: $\hat{Z}_{\mathrm{H}} = \hat{Z}_{\mathrm{e}}$ and $\hat{Z}_{\mathrm{H}} = \hat{Z}_{\mathrm{o}}$. The state $|+\rangle_{\mathrm{H}}$ precesses at twice the coupling rate between the two transmons in the microwave dual-rail qubit. A graphical representation of the hybrid qubit redundantly encoded with one microwave qubit and one optical qubit is shown in Fig. 5(a).

To produce resource states, we prepare multiple blocks (Fig. 3) in the state $|+\rangle_{\mathrm{H}}$. By applying a controlled-Z (CZ) gate between microwave qubits from different blocks, we can construct a graph state $G(E, V)$ of encoded hybrid qubits, defined as

$$|G\rangle = \prod_{(i,j)\in E} \mathrm{CZ}_{i,j} |+\rangle_{\mathrm{H}}^{\otimes V}. \tag{7}$$

Equivalently, the graph state $|G\rangle$ of k qubits can be described by its stabilizer generators,

$$\hat{X}_{i,\mathrm{H}} \prod_{j\in\mathcal{N}(i)} \hat{Z}_{j,\mathrm{H}} \text{ for all } i \in \{1, 2, \ldots, k\}, \tag{8}$$

where $\mathcal{N}(i)$ is the set of vertices in the neighborhood of vertex i. The action of $\mathrm{CZ}_{i,j}$ on two hybrid qubits i, j is

$$\hat{X}_{i,\mathrm{H}} \rightarrow \hat{X}_{i,\mathrm{H}}\hat{Z}_{j,\mathrm{H}}, \quad \hat{X}_{j,\mathrm{H}} \rightarrow \hat{Z}_{i,\mathrm{H}}\hat{X}_{j,\mathrm{H}}. \tag{9}$$

Using $\hat{X}_{\mathrm{H}} = \hat{X}_{\mathrm{e}}\hat{X}_{\mathrm{o}}$ and $\hat{Z}_{\mathrm{H}} = \hat{Z}_{\mathrm{o}}$, we see that application of CZ gates followed by measurement of the microwave dual-rail qubit in the X basis implements $\hat{X}_{i,\mathrm{H}} \rightarrow m_{i,\mathrm{e}}\hat{X}_{i,\mathrm{o}}\hat{Z}_{j,\mathrm{o}}$ and $\hat{X}_{j,\mathrm{H}} \rightarrow m_{j,\mathrm{e}}\hat{Z}_{i,\mathrm{o}}\hat{X}_{j,\mathrm{o}}$, where $m = \pm 1$ is the measurement outcome. Thus, up to a Pauli-frame correction given by the measurement outcomes, the quantum correlations that are left on the optical qubits are precisely those of a graph state. The microwave-optical hybrid qubits effectively allow us to teleport an arbitrary graph state prepared on the superconducting processor to optics using only single-qubit measurements.

As an example, Fig. 5(b) shows how we can construct a six-qubit hexagonal hybrid graph state (six-ring) represented by vertices V and edges E. An all-optical six-ring resource state can be extracted directly from the hybrid resource state by measuring all microwave qubits in the X basis. Alternatively, we may apply a Hadamard gate on an optical dual-rail qubit or a microwave dual-rail qubit to push this qubit out of its original vertex so that it forms a new vertex connected by an edge to its original vertex [75]. This is illustrated in the final graph state in Fig. 5(b), where we have applied a Hadamard gate on the microwave qubits. Measurement of the microwave qubits in the computational basis would remove them from the graph state, leaving an all-optical six-ring that can be used in a fusion-network implementation of a surface code with linear optics [12]. Other graph states, such as repeater graphs, can also be assembled deterministically, as illustrated in Fig. 5(c).

A consequence of the probabilistic heralding of the microwave-optical Bell pairs is that many blocks must be pumped simultaneously to obtain multiple pairs to combine into a resource state. Because it is random which blocks produce a microwave-optical Bell pair in any given RSG cycle, the microwave processor that performs entangling gates between such pairs benefits from tunable coupling between many blocks. Thus, our scheme synergizes with efforts to increase superconducting-qubit connectivity [76–78]. However, our scheme does not require this. For example, blocks in Fig. 3 that did not herald a state $|+\rangle_{\mathrm{H}}$ can be put in the state $|+_{\mathrm{e}}\rangle$ deterministically [40], and can then be used in the construction of the microwave-optical cluster state.

IV. PERFORMANCE ANALYSIS

The primary application of our scheme is the production of optical graph states using a superconducting processor and *imperfect* transducers. If transducers that could deterministically convert a microwave photon to an optical photon with negligible loss and added noise were available, the scheme presented would be less efficient than direct transduction of a graph state prepared on the superconducting processor. It is therefore of interest to investigate what level of performance would be required for our scheme and which metrics matter most to reach this level.

A. Squeezing and multiphoton noise

A fundamental feature of optomechanical two-mode squeezing is the production of states with two or more photons from a single laser pulse. Such states are unwanted, and we refer to them as "multiphoton noise." This noise sets an upper bound on how hard we can squeeze the transducer, regardless of its imperfections, such as thermal noise and photon loss, since the contribution of multiphoton states to $|\psi\rangle$ in Eq. (3) grows as we squeeze harder. However, squeezing too weakly implies that the heralding probability p for a microwave-optical Bell state becomes prohibitively low. The size of the superconducting processor required for reliable generation of resource states is inversely proportional to p, and the need for long-range connections between transmons becomes more pressing for low values of p. Without access to a long-lived quantum memory, $p \lesssim 1\%$ is too low.

In the protocol described in Sec. III, controlling the swap time between the transducer and the transmon allows us to take advantage of the different swap speeds of the one-photon and two-phonon states to suppress noise from the latter. A QuTiP simulation [79] of a transmon and a piezo-optomechanical transducer during squeezing and subsequent swap operation is shown in Fig. 6. Here, the two-phonon state is almost completely swapped back to the mechanical mode. At the same time, the one-phonon state is almost completely swapped to the transmon. This ensures that when the parity check heralds the state $|+\rangle_H$, the probability of finding two optical photons in the optical dual-rail qubit is suppressed. This allows us to squeeze the transducer harder without substantially increasing multiphoton noise in the heralded logical qubits until three-photon contributions become relevant. The microwave-optical heralding probability when a transducer is pumped as shown in Fig. 6 is 19%.

B. Hardware imperfections

We now turn to the effects of nonideal hardware. These will naturally depend on the choice of superconducting processor and transducer type used to implement the scheme. We continue to focus on transmon qubits and
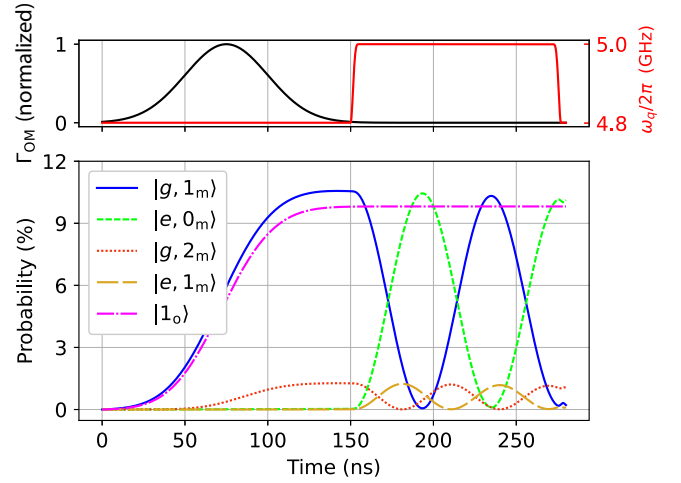

FIG. 6. Time-domain microwave-optical squeezing along with electromechanical swap and multiphoton noise filtering. Simulated populations (bottom) of the transmon and mechanical mode during the Gaussian pump pulse and subsequent swap to the transmon (top). Shown in pink is the probability of finding one optical photon in the corresponding optical wave packet leaving the transducer, after the transmon and mechanical mode have been traced out. See Appendix B for details of the simulation.

piezo-optomechanical transducers for concreteness. Our approach is to simulate a single rail in the dual-rail qubit using QuTiP [79] as we pump the transducer and swap the phonons to the transmon. We construct the density matrix of a microwave-optical dual-rail qubit before the parity check by taking the tensor product of two of the simulated rails: $\hat{\rho}_{DR} = \hat{\rho}_{R1} \otimes \hat{\rho}_{R2}$. We then perform the parity check by measuring $\hat{Z}_{q,R1}\hat{Z}_{q,R2}$, where $\hat{Z}_q$ is the Pauli-Z operator on the physical transmon qubit. Details of the simulations can be found in Appendix B.

We analyze three parameter regimes for the piezo-optomechanical transducer detailed in Table I. First, we take the transducer design from Ref. [66] and find a Bell-state fidelity $F = \text{Tr}\left(\hat{\rho}_{DR}|+\rangle_H\langle+|\right)$ of just 38% after heralding. Second, we run the same simulation with a transducer that has been better tailored to our scheme. In particular, we assume optical quality factors at half the value of state-of-the-art silicon photonic crystals [80]—roughly a quarter of the theoretical disorder-free scattering upper limit of a demonstrated OMC [81]—as well as stronger coupling of the mechanical mode to the fridge bath and increased piezoelectric interaction strength. In this case, we find that the postheralding fidelity increases to 81%. Third, we reduce the thermal noise in the transducer and find a fidelity of 88%. While they capture the overall quality of the generated optical states, these Bell-state fidelities do not describe the error mechanisms or the error budget. In the following, we summarize the main sources of error and estimate the performance of each

TABLE I.   Parameters used in simulations of a piezo-optomechanical transducer during microwave-optical Bell-state preparation. In addition to the design from Ref. [66], we perform simulations using piezo-optomechanical transducers with improvements in three key parameters: optical quality factor, mechanical mode heating, and electromechanical coupling. The optical quality factor and heating are the dominant factors determining the fidelity of the heralded Bell pairs. Electromechanical coupling has a much smaller impact on fidelity, but weak coupling leads to slower operation of the RSG and more Pauli errors.

Parameter	Symbol	Current design [66]	Improved design	FBQC design
Mechanical mode frequency	ω_m	$2\pi \times 5\,\text{GHz}$	$2\pi \times 5\,\text{GHz}$	$2\pi \times 5\,\text{GHz}$
Electromechanical coupling	g_{qm}	$2\pi \times 3\,\text{MHz}$	$2\pi \times 6\,\text{MHz}$	$2\pi \times 6\,\text{MHz}$
Mechanical coupling to cold fridge bath	γ_0	$2\pi \times 10\,\text{KHz}$	$2\pi \times 100\,\text{KHz}$	$2\pi \times 100\,\text{KHz}$
Mechanical coupling to hot phonon bath	γ_b	$2\pi \times 10\,\text{KHz}$	$2\pi \times 10\,\text{KHz}$	$2\pi \times 10\,\text{KHz}$
Mechanical dephasing rate	γ_ϕ	$2\pi \times 10\,\text{KHz}$	$2\pi \times 10\,\text{KHz}$	$2\pi \times 10\,\text{KHz}$
Hot-phonon-bath turn-on rate[a]	γ_s	$2\pi \times 215\,\text{KHz}$	$2\pi \times 215\,\text{KHz}$	$2\pi \times 215\,\text{KHz}$
Slow-growing fraction of hot phonon bath[a]	δ	0.8	0.8	0.8
Steady-state phonon-bath occupancy[a]	n_b	20	5	1
Single-photon optomechanical coupling rate	g_0	$2\pi \times 830\,\text{KHz}$	$2\pi \times 830\,\text{KHz}$	$2\pi \times 830\,\text{KHz}$
Peak optomechanical coupling rate	$\max G(t)$	$2\pi \times 5.5\,\text{MHz}$	$2\pi \times 9\,\text{MHz}$	$2\pi \times 9\,\text{MHz}$
Gaussian-pump-pulse duration (s.d.)	τ_{pulse}	25 ns	25 ns	25 ns
Optical coupling to waveguide	κ_{ex}	$2\pi \times 1\,\text{GHz}$	$2\pi \times 1\,\text{GHz}$	$2\pi \times 1\,\text{GHz}$
Intrinsic optical loss rate	κ_{int}	$2\pi \times 400\,\text{MHz}$	$2\pi \times 40\,\text{MHz}$	$2\pi \times 40\,\text{MHz}$
Transmon frequency (detuned)	$\omega_q(0)$	$2\pi \times 4.8\,\text{GHz}$	$2\pi \times 4.8\,\text{GHz}$	$2\pi \times 4.8\,\text{GHz}$
Transmon-frequency rise time (fall time)	T_r (T_f)	5 ns	5 ns	5 ns
Transmon charging energy (in the unit of h)	E_C	200 MHz	200 MHz	200 MHz
Transmon-energy decay time	T_1	$100\,\mu\text{s}$	$100\,\mu\text{s}$	$100\,\mu\text{s}$
Transmon dephasing time	T_ϕ	$100\,\mu\text{s}$	$100\,\mu\text{s}$	$100\,\mu\text{s}$
Thermal-photon-bath occupancy	n_a	0.1	0.1	0.1
Simulated fidelity to $|+\rangle_H$	F	38%	81%	88%

[a]Heating model for the optomechanical crystal in Ref. [82].

hardware component that would be necessary to reach the fault-tolerance threshold.

Most dual-rail-qubit errors take the qubit out of the logical subspace. Such errors lead to qubit erasure and are relatively benign, with error-correction thresholds in fault-tolerant fusion networks and cluster states on the order of 10% [11,41,83]. In contrast, Pauli-error thresholds are currently only around 1% [12,84]. Therefore, it is necessary to analyze the main sources of Pauli and erasure errors separately.

1. Pauli errors

Pauli errors may arise from dephasing of the dual-rail qubit. Dual-rail qubits can have longer coherence times than their constituent superconducting qubits through hard-coded noise suppression [39,40,63]. Decay and dephasing times of about 1 ms have been demonstrated for dual-rail qubits with the use of transmon qubits with $T_1 \sim 20\,\mu\text{s}$ [40] and have not exhausted the limits of this technique. Another source of Pauli error is mechanical dephasing during the 250 ns before the swap to the superconducting qubit is complete (Fig. 6). Cutting-edge OMCs support dephasing times on the order of $100\,\mu\text{s}$ [59]. Performance close to that may be reached in piezo-optomechanical structures by, for example, shrinking the piezoelectric section [30,33,66]. The average number of

phonons in our heralding protocol is only approximately 0.1, reducing the mechanical dephasing rate.

The parity check that heralds a microwave-optical Bell pair may give an erroneous result. This could lead to Pauli errors when we implement two-qubit gates on microwave dual-rail qubits that are outside the computational space. However, imperfect discrimination of the even-parity and odd-parity states will be detected when the dual-rail qubit is measured. We can then erase all affected qubits from the resource state before it is used in an implementation of a topological error-correcting code [48]. This is in contrast to proposals where the dual-rail qubits are used directly in circuit-based implementations of, for example, the surface code [39]. Moreover, fusion measurements on the resource states deterministically detect leakage, allowing us to treat leakage equivalently to loss. Pauli errors from measurement errors are strongly suppressed because both rails in the dual-rail qubit are measured. If the measurements are inconsistent, we similarly erase the qubit from the resource state.

2. Erasure errors

The two leading sources of erasure error are optical photon loss and mechanical thermal noise. Photons are lost due to absorption and scattering in the microwave-optics transducer. Intrinsic optical quality factors above

TABLE II.   Error budget for microwave-optical Bell state preparation. Overlaps of the simulated state produced from a single block in our scheme with selected candidate states after heralding, and the observed error on the optical dual-rail qubits. Simulation parameters are from Table I.

State	Current design [66]	Improved design	FBQC design	Error observed
$\lvert+\rangle_{\mathrm{H}}$	0.380	0.810	0.883	
$(\lvert g0\rangle_{\mathrm{R1}}\lvert e0\rangle_{\mathrm{R2}} \pm \lvert e0\rangle_{\mathrm{R1}}\lvert g0\rangle_{\mathrm{R2}})) /\sqrt{2}$	0.614	0.130	0.059	Photon loss
$(\lvert g0\rangle_{\mathrm{R1}}\lvert e2\rangle_{\mathrm{R2}} \pm \lvert e2\rangle_{\mathrm{R1}}\lvert g0\rangle_{\mathrm{R2}})) /\sqrt{2}$	0.002	0.023	0.022	Multiphoton noise
$(\lvert g1\rangle_{\mathrm{R1}}\lvert e1\rangle_{\mathrm{R2}} \pm \lvert e1\rangle_{\mathrm{R1}}\lvert g1\rangle_{\mathrm{R2}})) /\sqrt{2}$	0.001	0.010	0.010	Multiphoton noise
$(\lvert g0\rangle_{\mathrm{R1}}\lvert e3\rangle_{\mathrm{R2}} \pm \lvert e3\rangle_{\mathrm{R1}}\lvert g0\rangle_{\mathrm{R2}})) /\sqrt{2}$	<0.001	0.010	0.011	Multiphoton noise
$(\lvert g2\rangle_{\mathrm{R1}}\lvert e1\rangle_{\mathrm{R2}} \pm \lvert e1\rangle_{\mathrm{R1}}\lvert g2\rangle_{\mathrm{R2}})) /\sqrt{2}$	<0.001	0.008	0.009	Multiphoton noise
$(\lvert g0\rangle_{\mathrm{R1}}\lvert e1\rangle_{\mathrm{R2}} - \lvert e1\rangle_{\mathrm{R1}}\lvert g0\rangle_{\mathrm{R2}})) /\sqrt{2}$	0.001	0.006	0.005	Phase flip

2×10^6 can keep this error below 10% given common external coupling rates of 1 GHz. Piezo-optomechanical transducers [29,33,59,82] may reach this value given the order-of-magnitude improvements in optical quality that have already been demonstrated in similar photonic crystals [80]. So far, transducers have not explicitly been optimized with this goal in mind.

Thermal noise in the mechanics or qubits can falsely herald the excitation of a Bell pair. This will produce the same state as a correctly heralded Bell pair followed by optical photon loss. Therefore, it is important that the mechanical mode is in its ground state at the beginning of each clock cycle, and that optical absorption [59] does not heat up the mechanical mode appreciably before its phonons are swapped to the superconducting qubit. Pristine silicon OMCs heat up slowly enough that the heating can be tolerated on the timescale of Bell-state preparation [59,81]. However, the addition of piezoelectric elements currently causes the mechanical mode to heat up within 100 ns [29,66]. Designing the mechanical mode to be predominantly siliconlike may reduce the heating to close to that of OMCs [66]. Qubit erasure errors from thermal noise can then be kept below 10%.

C. Error hierarchy

As a concrete example of how hardware imperfections cause errors on the microwave-optical dual-rail qubits, Table II shows the breakdown of the simulated density matrices ρ_{DR} after the parity check in terms of overlap with states that constitute errors on the qubits. The simulated error rates can be reduced by optimization of the squeezing strength to suit the performance of the transducer, particularly for the improved design, where multiphoton noise is significant despite the proposed noise filtering (Fig. 6). The observed photon loss rate with the best-performing transducer in Table II is below the threshold set by fusion erasure for FBQC with six-ring resource states [12], but the threshold must be increased further to tolerate multiphoton noise, Pauli errors, and fusion failure. This can be

achieved with loss-tolerant encoding [12,41] and dynamic bias arrangement [85].

Dual-rail microwave-optical qubits have an error hierarchy very similar to that found for all-microwave dual-rail qubits [38,39]. In Fig. 7, we give an overview of feasible hardware performance in terms of errors on the optical qubits produced by the RSG, ranging from pessimistic with little improvement over current devices to optimistic with a transducer that combines state-of-the-art performance for the transmon, optical quality factor similar to that of all-optical silicon photonic crystals [80], and thermal noise levels of state-of-the-art optomechanical crystals.

D. Quasiparticle poisoning of superconductors

We conclude the performance analysis with a note on the integration of superconducting circuits and optics. Stray optical pump photons can excite quasiparticles in superconductors that temporarily reduce the lifetime of transmon qubits [29,87]. While our scheme does not rely on the preservation of a transmon's quantum state during the optical pulse, it is important that the transmons operate with high coherence within approximately 10ns after the pump pulse. Otherwise, swapping of the mechanical state to the superconducting qubit is not possible. The use of only superconductors with short quasiparticle lifetimes or shielding of the superconducting qubits from optical radiation through, for example, infrared filtering may address this issue. Gap engineering of the Josephson junction in aluminum transmons was recently found to increase the tolerance to optical illumination by more than three orders of magnitude [88]. We expect that combining gap engineering of the aluminum Josephson junction with low-quasiparticle-lifetime materials for the rest of the microwave circuitry will yield sufficiently light-insensitive qubits to run the protocols described here.

V. FAULT-TOLERANCE OVERHEAD

Fault-tolerant quantum technologies typically come with a steep cost in overhead once the performance of the

hardware can be kept below the relevant thresholds. In general, the overhead needed to reach a target performance level depends on how far below the threshold the hardware is performing. Finding precise error thresholds for FBQC with microwave-optical RSGs is beyond the scope of this proposal. In this section, we compare the overhead of FBQC with microwave-optical RSGs with other candidate fault-tolerant schemes, assuming that the performance is just barely below the fault-tolerance threshold for all schemes. The aim is to estimate, on the basis of the fundamental working principles of each approach, how costly FBQC with our RSGs is compared with established alternatives.

A. Comparison with all-optical schemes

To illustrate how efficient our scheme can be for producing optical resource states, we compare the number
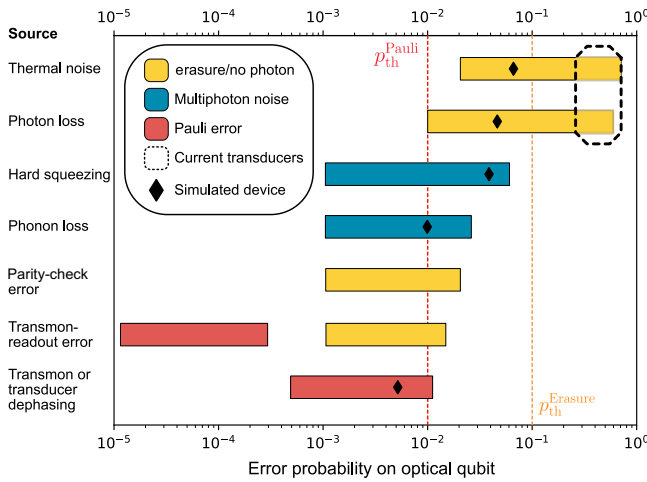

FIG. 7. Error hierarchy of the entangled optical qubits produced by the RSG. The bars represent feasible error rates from the dominant error sources, from pessimistic estimates based on currently available transducers to optimistic estimates based on, for example, theoretical disorder-free performance limits of current optomechanical crystals [81] and experimentally demonstrated silicon photonic crystals [80]. The performance of the simulated improved transducer ($F = 81\%$) is indicated in Table I. The simulation does not give the source of the observed errors, and therefore the indicated values are associated with some uncertainty. The parity check in our simulation is error-free and therefore not indicated. This has little effect on the overall error on the qubit because errors from microwave thermal noise and optical photon loss dominate. Transmon readout is not part of our simulation but is also expected to be a minor contribution to both erasure and Pauli errors. Dashed lines represent known fault-tolerance thresholds obtained with error models for linear optical quantum computation [12,41,84–86] and should be interpreted as estimates for the thresholds for FBQC using the proposed RSGs. Multiphoton noise will contribute predominantly to erasure, but a fraction could also be turned into Pauli error if photons are lost at a later stage.

of blocks needed to produce the six-ring [Fig. 5(b)] for a fault-tolerant fusion network [12] with the equivalent number of optical photons required with linear optics. While this is an open research problem in classical and quantum photonics, we assume that for the latter case a fast and low-loss optical switch can be produced so that optical photons can be multiplexed—which is required for an all-optical approach [89,90]. A six-ring can be made from three copies of a three-qubit linear cluster state, which is locally equivalent to a Greenberger-Horne-Zeilinger (GHZ) state, with the use of type-I fusion [10]. All-optical circuits can ballistically produce GHZ states from six photons with probability $1/2^5$ with perfect photon number–resolving detectors [11]. Therefore, the average number of photons needed to produce a GHZ state is 192. Fusing three such states with type-I fusion gates, each with probability of success 1/2, increases the average number of photons needed to make a six-ring to 4608 if states that underwent failed fusion are discarded. In contrast, our scheme would not need extra photons to entangle qubits, and the entangling gates are deterministic. The number of microwave-optical Bell pairs required to create a six-ring is six, but because each block produces a Bell pair with limited probability p, the number of blocks needed to reliably produce such states is $2 \times 6/p$, where p is the probability of heralding a microwave-optical Bell pair from a single block. We estimate that p can reach 20% with the scheme and architecture presented in this work. Higher heralding probabilities would likely generate too much multiphoton noise from the strong squeezing required.

The six-ring or other resource states for fusion networks will likely need to be concatenated with a graph code to increase tolerance to photon loss and fusion failure [41]. As the size of the resource state is scaled up, the overhead implied by the probabilistic linear optical generation of such states increases rapidly. With our scheme, the overhead scales linearly with the size of the resource state. Moreover, our scheme circumvents the need for large-scale switching of photons for resource-state generation. With lossy switches, minimizing the switch depth is crucial.

Besides the favorable scaling with resource-state size compared with the scaling for linear optics, the utility of our scheme also depends on its repetition rate. Current piezo-optomechanical transducers are limited by heating to rates on the order of 10 kHz [30, 33,66]. Optomechanical crystals with improved thermal anchoring are under investigation to address this issue [81,91]. Several other transducer types, each with their benefits and challenges, are under development [28–33,52,65]. Improved transducers may relax or even completely remove the heating constraint, allowing resource-state generation rates to approach the limit set by the microwave gate times—estimated to be on the order of 1 MHz. Such repetition rates would make a single

RSG cycle similar to a surface code cycle on a traditional superconducting processor.

B. Comparison with all-microwave schemes

For long-term applications, we now estimate how many RSGs would be required to match the computational power of a superconducting processor on its own. The use of superconducting qubits to build RSGs rather than a surface-code processor will incur an overhead because the heralding of the microwave-optical Bell pairs is probabilistic and noisy. This overhead could leave the modular approach presented here at a disadvantage compared with scaling the size of the superconducting processor to hundreds of thousands of qubits, assuming this could be done without optics. We argue that construction of a fusion-based quantum computer is not as costly as it might appear thanks to the power of low-loss-optical-fiber delay lines. In a surface code of distance d, the number of logical qubits that can be encoded with one RSG is given by [92]

$$N_{\text{L}} = \frac{\Gamma_{\text{RSG}} t_{\text{d}}}{d^2}, \tag{10}$$

where Γ_{RSG} is the resource-state generation rate and t_{d} is the maximum delay time from when a resource state is generated until all its qubits have been measured. If $t_{\text{d}} = 10\,\mu\text{s}$, then optical qubits stored in commercially available fiber with a loss rate of 0.16 dB/km [93] suffer only 7% additional loss. This extra delay loss affects only a few photons, and the delay loss can therefore exceed the threshold for baseline loss—i.e., the photon loss considered in this paper—without lowering this threshold substantially [37]. We assume for the purpose of illustration that it takes 100 dual-rail qubits to build one RSG and that each RSG cycle takes $1\,\mu\text{s}$. Then $N_{\text{L}} = 10/d^2$, and each superconducting dual-rail qubit contributes $1/10d^2$ towards a logical qubit. The equivalent number for a dual-rail qubit on a superconducting processor with the use of the rotated surface code is $1/2d^2$, so the additional overhead for our proposal in this example is a factor of 5. This is before we have accounted for the overhead reductions that LDPC codes and an active-volume architecture might bring.

A future full-stack comparison could also take into account that microwave systems do not easily scale beyond about 1000 qubits [94] in a single cryogenic system with current schemes. Thus, optics is likely needed either way to scale up microwave qubits to fault tolerance through optically heralded microwave entanglement [43,44]. Alternative microwave approaches using tailored delay lines [54] and LDPC codes [53] are, as for microwave-optics devices, in an early stage of development. Their advantage lies in deterministic entanglement generation [54], and their challenge lies in long-range connectivity [53].

Optics has long been the preferred information carrier in classical nonlocal interconnects and is taking over from microwaves in data centers as well as between and eventually within electronic chips. One may expect this trend to continue both within and between quantum processors of any kind.

VI. CONCLUSION

We propose a scheme for generating microwave-optical cluster states of dual-rail encoded qubits. Our architecture uses imperfect quantum transducers as sources of microwave-optical Bell pairs. Next, it deterministically entangles Bell pairs into cluster states. Single-qubit measurements of the microwave qubits reduce the hybrid cluster states to all-optical resource states, thus teleporting an arbitrary graph state prepared on the superconducting processor to optics. Deterministic entanglement generation in the microwave domain allows our scheme to produce optical resource states faster than equivalent schemes in linear optics, even if individual optical photons could be generated at rates orders of magnitude higher. Although the analysis focuses on generating entangled optical photons from a microwave processor, this work is only a first step in exploring the landscape of architectures harnessing hybrid microwave-optical qubits. The proposed scheme can be used to turn microwave-frequency superconducting processors into resource-state generators useful for fault-tolerant quantum communication, computation, and sensing. Improved isolation of qubits from stray light would place the scheme within reach of proof-of-principle demonstrations with current hardware.

Research into hybrid microwave-optics devices is accelerating. If they continue to improve on their current steep path, and are tailored to the proposed scheme, we predict that fault-tolerance thresholds are within reach and will eventually be surpassed. This would enable the combination of the exquisite quantum control of microwave circuits with the nonlocal connectivity of optics. The scheme is competitive with the low-connectivity all-microwave approach even when the constraint of a single cryogenic system is hypothetically removed. Initially, the benefits of this approach will likely be felt most in situations where the leading information carriers are optical photons either way. This includes long-distance networking, optical quantum sensing and computing, and scaling up microwave processors well beyond one cryogenic system.

APPENDIX A: TWO-MODE SQUEEZING OF AN OPEN OPTOMECHANICAL SYSTEM

We investigate the optomechanical squeezing responsible for creating the entangled phonon-photon pair that we use to create a microwave-optical Bell pair. During the pump pulse, the mechanical mode is dispersively coupled to the qubit. The Hamiltonian of the system can then be approximated [29,95] as $\hat{H} = \hat{H}_0 + \hat{H}_{\text{int}}$, with

$$\hat{H}_0 = \frac{1}{2}\hbar\omega_{\text{q}}(0)\hat{\sigma}^z + \hbar\omega_{\text{m}}\hat{b}^\dagger\hat{b} + \hbar\chi\hat{b}^\dagger\hat{b}\hat{\sigma}^z - \hbar\omega_{\text{m}}\hat{c}^\dagger\hat{c},$$

$$\text{(A1)}$$

$$\hat{H}_{\text{int}} = \hbar G(t)\left(\hat{b}^\dagger\hat{c}^\dagger + \hat{b}\hat{c}\right),$$

$$\text{(A2)}$$

where $\hbar$ is the reduced Planck constant, $\omega_{\text{q}}(0)$ is the qubit frequency before the swap with the mechanical mode, ω_{m} is the frequency of the mechanical mode, $G(t)$ is the optomechanical coupling strength, $\hat{\sigma}^z = |e\rangle\langle e| - |g\rangle\langle g|$ is the Pauli-Z matrix, $\hat{\sigma}^+$ ($\hat{\sigma}^-$) is the qubit raising (lowering) operator, $\hat{b}^\dagger$ ($\hat{b}$) is the mechanical mode creation (annihilation) operator, and $\hat{c}^\dagger$ ($\hat{c}$) is the optical mode creation (annihilation) operator. We have defined the mechanical frequency shift depending on the state of the qubit,

$$\chi = -\frac{g_{\text{qm}}^2 E_{\text{C}}/\hbar}{\Delta\left(\Delta - E_{\text{C}}/\hbar\right)} \ll \omega_{\text{m}},$$

$$\text{(A3)}$$

with E_{C} the charging energy of the superconducting qubit and $\Delta = \omega_{\text{q}}(0) - \omega_{\text{m}} \gg g_{\text{qm}}$ the qubit-mechanics detuning [2,58].

We assume that the qubit remains in the ground state during the pump pulse such that the qubit state and the optomechanical state factorize, $\rho(t) = \rho_{\text{q}}(0) \otimes \rho_{\text{OM}}(t)$. Absorbing the qubit-induced mechanical frequency shift $\omega_{\text{m}} - \chi/2 \to \omega_{\text{m}}$ and moving to a frame rotating at the mechanical frequency, we find that the Heisenberg-Langevin equations for the optomechanical system are

$$\dot{\hat{c}} = -\frac{\kappa}{2}\hat{c} + iG(t)\hat{b}^\dagger + \sqrt{\kappa}\hat{c}_{\text{in}},$$

$$\text{(A4)}$$

$$\dot{\hat{b}} = -\frac{\gamma}{2}\hat{b} + iG(t)\hat{c}^\dagger + \sqrt{\gamma}\hat{b}_{\text{in}},$$

$$\text{(A5)}$$

where κ is the total optical linewidth and γ is the total mechanical linewidth. We have defined the standard input

fields [96] to the optical and mechanical modes as $\hat{c}_{\text{in}}$ and $\hat{b}_{\text{in}}$, respectively. The input operators in Eqs. (A4) and (A5) obey the standard commutation relations [96]

$$\left[\hat{b}_{\text{in}}(t), \hat{b}_{\text{in}}^\dagger(t')\right] = \left[\hat{c}_{\text{in}}(t), \hat{c}_{\text{in}}^\dagger(t')\right] = \delta(t - t').$$

$$\text{(A6)}$$

We exploit the fact that $\kappa \gg G(t)$ at all times to approximate the optical response as instantaneous, setting $\dot{\hat{c}} = 0$ in Eq. (A4). This yields the coupled equations

$$\hat{c} = i\sqrt{\frac{\Gamma_{\text{OM}}}{\kappa}}\hat{b}^\dagger + \frac{2}{\sqrt{\kappa}}\hat{c}_{\text{in}},$$

$$\text{(A7)}$$

$$\dot{\hat{b}} = -\frac{\gamma - \Gamma_{\text{OM}}}{2}\hat{b} + i\sqrt{\Gamma_{\text{OM}}}\hat{c}_{\text{in}}^\dagger + \sqrt{\gamma}\hat{b}_{\text{in}},$$

$$\text{(A8)}$$

where $\Gamma_{\text{OM}}(t) = 4G(t)^2/\kappa$ is the optomechanical scattering rate. We can solve Eq. (A8) analytically for the case of a square pump pulse of duration τ. Direct integration over the pump pulse yields

$$\hat{b}(\tau) = e^{\frac{\Gamma_{\text{OM}}-\gamma}{2}\tau}\hat{b}(0)$$

$$+ i\sqrt{\Gamma_{\text{OM}}}e^{\frac{\Gamma_{\text{OM}}-\gamma}{2}\tau}\int_0^\tau dt\, e^{-\frac{\Gamma_{\text{OM}}-\gamma}{2}t}\hat{c}_{\text{in}}(t)$$

$$+ \sqrt{\gamma}e^{\frac{\Gamma_{\text{OM}}-\gamma}{2}\tau}\int_0^\tau dt\, e^{-\frac{\Gamma_{\text{OM}}-\gamma}{2}t}\hat{b}_{\text{in}}(t). \quad \text{(A9)}$$

We now write $\gamma = \alpha\Gamma_{\text{OM}}$. Optomechanical devices are often operated in the high-cooperativity regime, where $\mathcal{C} = \Gamma_{\text{OM}}/\gamma \gg 1$ (or equivalently $\alpha \ll 1$) [59,82,95] such that the coherent readout occurs faster than the mechanical decoherence. However, for our scheme we are more likely to be in the regime where $\alpha \sim 1$ because we want phonons to leak out before the next clock cycle of our protocol is started. By defining the operators [68]

$$\hat{C}_{\text{in}} = \sqrt{\frac{(1-\alpha)\Gamma_{\text{OM}}}{1 - e^{(\alpha-1)\Gamma_{\text{OM}}\tau}}}\int_0^\tau dt\, e^{-\frac{(1-\alpha)\Gamma_{\text{OM}}t}{2}}\hat{c}_{\text{in}}(t), \quad \text{(A10)}$$

$$\hat{C}_{\text{out}} = \sqrt{\frac{(1-\alpha)\Gamma_{\text{OM}}}{e^{(1-\alpha)\Gamma_{\text{OM}}\tau} - 1}}\int_0^\tau dt\, e^{\frac{(1-\alpha)\Gamma_{\text{OM}}t}{2}}\hat{c}_{\text{out}}(t), \quad \text{(A11)}$$

and using the well-known input-output relation $\hat{c}_{\text{out}} = -\hat{c}_{\text{in}} + \sqrt{\kappa}\hat{c}$, we have to lowest order in $\Gamma_{\text{OM}}\tau$

$$\hat{C}_{\text{out}} = e^{\frac{(1-\alpha)\Gamma_{\text{OM}}\tau}{2}}\hat{C}_{\text{in}} + \frac{i}{\sqrt{1-\alpha}}\sqrt{e^{(1-\alpha)\Gamma_{\text{OM}}\tau} - 1}\hat{b}^\dagger(0),$$

$$\text{(A12)}$$

$$\hat{b}(\tau) = e^{\frac{(1-\alpha)\Gamma_{\text{OM}}\tau}{2}}\hat{b}(0) + \frac{i}{\sqrt{1-\alpha}}\sqrt{e^{(1-\alpha)\Gamma_{\text{OM}}\tau} - 1}\hat{C}_{\text{in}}^\dagger + \hat{F}.$$

$$\text{(A13)}$$

The operator

$$\hat{F} = \sqrt{\gamma}e^{\frac{(1-\alpha)\Gamma_{OM}}{2}\tau} \int_0^\tau dt\, e^{-\frac{(1-\alpha)\Gamma_{OM}}{2}t}\hat{b}_{in}(t) \qquad \text{(A14)}$$

represents the noise coming from the coupling to the thermal-phonon bath. To lowest order in $\Gamma_{OM}\tau$, we have $\left[\hat{C}_{in}, \hat{C}_{in}^\dagger\right] = \left[\hat{C}_{out}, \hat{C}_{out}^\dagger\right] = 1$ and $\left[\hat{F}, \hat{F}^\dagger\right] = \gamma\tau$. Our scheme *requires* $\Gamma_{OM}\tau \ll 1$ to keep the probability of exciting multiple phonon-photon pairs low, so keeping only lowest-order terms is a good approximation.

In the absence of mechanical noise, we see that in the limit $\gamma \to 0$ ($\alpha \to 0$), corresponding to high mechanical quality factors, Eqs. (A12) and (A13) represent two-mode squeezing of the mechanical mode and the output optical field with $e^{\Gamma_{OM}\tau/2} = \cosh(r)$ and $\sqrt{e^{\Gamma_{OM}\tau} - 1} = \sinh(r)$. However, even when $\alpha \approx 1$, we get a similar behavior. We have

$$\lim_{\alpha \to 1} \sqrt{\frac{e^{(1-\alpha)\Gamma_{OM}\tau} - 1}{1-\alpha}} = \sqrt{\Gamma_{OM}\tau}, \qquad \text{(A15)}$$

and with $\Gamma_{OM}\tau \lesssim 10^{-1}$, the relevant order of magnitude for our scheme, we obtain

$$\hat{C}_{out} = \hat{C}_{in} + i\sqrt{\Gamma_{OM}\tau}\hat{b}^\dagger(0), \qquad \text{(A16)}$$

$$\hat{b}(\tau) = \hat{b}(0) + i\sqrt{\Gamma_{OM}\tau}\hat{C}_{in}^\dagger \qquad \text{(A17)}$$

to order $\sqrt{\Gamma_{OM}\tau}$, regardless of whether α is close to unity or much smaller than unity. If $\alpha \gg 1$ (i.e., $\gamma \gg \Gamma_{OM}$), then we no longer have something that resembles two-mode squeezing because the phonons in the mechanical mode escape faster than we can produce them.

In the above, we ignored thermal noise in the mechanics. Such noise would increase the mechanical dephasing rate and increase the required optomechanical cooperativity and scattering rate proportionally to the mechanical noise occupancy. Like many other quantum optomechanical protocols, we require the quantum cooperativity to exceed unity [59,68,82,95]. This requirement limits the repetition rate of today's piezo-optomechanical transducers.

APPENDIX B: SIMULATION OF BELL-STATE PREPARATION

We simulate the evolution of the state of the piezo-optomechanical transducer during microwave-optical entangled-state preparation using a Lindblad master equation [96]. The superconducting qubit is treated as an anharmonic oscillator rather than a two-level system when we tune its frequency in and out of resonance with the mechanics. To capture down-converted optical photons leaving the optical cavity inside the transducer, we use the formalism in Ref. [97], in which a virtual cavity interacts with the optical cavity. By choosing an appropriate coupling parameter $g_v(t)$ between the optical cavity and the virtual cavity, photons from the optical cavity will be absorbed by the virtual cavity and will not leak back into the optical cavity [97]. The virtual cavity acts as the output mode from the transducer with which the mechanical mode is entangled. The mode structure and the coupling between the modes are shown in Fig. 8.

As a consequence of the fast response of the optical cavity compared with the optomechanical squeezing interaction ($\kappa \gg G(t)$), the output wave packet from the optical mode is well approximated by the shape of the pump pulse. To absorb the output from the optical cavity, the complex coupling between the virtual cavity and the optical cavity is given by

$$g_v(t) = -\frac{v^*(t)}{\int_0^t dt'|v(t')|^2}, \qquad \text{(B1)}$$

where

$$v(t) \propto \exp\left[-\frac{(t-t_\mu)^2}{4\tau_{pulse}^2}\right]\exp(-i\omega_m t) \qquad \text{(B2)}$$

is approximately the shape of the output wave packet from the optical cavity in the rotating frame of the laser pump. Here, t_μ is the center of the laser pulse and τ_{pulse} is the standard deviation of the pulse.

The master equation takes the form

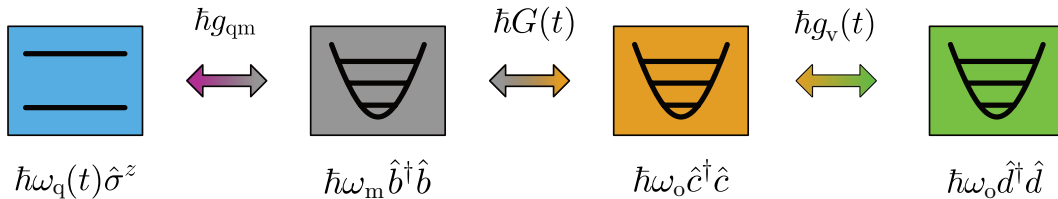$$\dot{\rho}(t) = \mathcal{L}(t)\hat{\rho}(t), \qquad \text{(B3)}$$

FIG. 8.   The modes in the QuTiP simulation and their interaction. From left to right, we have the transmon qubit, the mechanical mode in the transducer, the optical cavity in the transducer, and a virtual cavity to capture the emission from the optical cavity. The transmon qubit is treated as an anharmonic oscillator when simulated, to include contributions from the higher-excitation states.

where $\hat{\rho}$ is the combined state of the superconducting qubit, the mechanical transducer mode, the optical cavity, and the virtual cavity representing the entangled waveguide mode (Fig. 8). The master equation can be written in Lindblad form as

$$\frac{d\hat{\rho}}{dt} = -\frac{i}{\hbar}\left[\hat{H} + \hat{H}', \hat{\rho}(t)\right] + \sum_{i=0}^{n} \mathcal{D}\left[\hat{L}_i(t)\right]\hat{\rho}(t), \quad (B4)$$

where

$$\hat{H} = \hbar\omega_q(t)\hat{a}^\dagger\hat{a} - \frac{E_C}{2}\hat{a}^\dagger\hat{a}^\dagger\hat{a}\hat{a} + \hbar\omega_m\left(\hat{b}^\dagger\hat{b} - \hat{c}^\dagger\hat{c}\right)$$
$$+ \hbar g_{qm}\left(\hat{a} + \hat{a}^\dagger\right)\left(\hat{b} + \hat{b}^\dagger\right) \quad (B5)$$

is the Hamiltonian describing the transducer coupled to a superconducting qubit with charging energy E_C, which determines its anharmonicity [58], and

$$\hat{H}' = \frac{i\hbar}{2}\sqrt{\kappa}g_v^*(t)\hat{c}^\dagger\hat{d} - \text{H.c.} \quad (B6)$$

describes the coupling between the optical and virtual cavities. The sum over superoperators $\mathcal{D}(\hat{L}_i)\hat{\rho} = \hat{L}_i\hat{\rho}\hat{L}_i^\dagger - 1/2\left\{\hat{L}_i^\dagger\hat{L}_i, \hat{\rho}\right\}$ includes the dissipator

$$\hat{L}_0 = \sqrt{\kappa}\hat{c} + g_v^*\hat{d}. \quad (B7)$$

For an appropriate choice of $g_v(t)$, the optical cavity and virtual-cavity modes will evolve as a dark state of this dissipator. We include other jump operators $\hat{L}_i$ representing the incoherent interaction of the transducer with its environment. We use the model introduced by Meenehan *et al.* [82] for the time evolution of the mechanical mode population n while the optical pump is turned on:

$$\langle\dot{n}\rangle = (-\gamma + \Gamma_{OM})\langle n\rangle + \gamma_b n_b\left(1 - \delta e^{-\gamma_s t}\right) + \Gamma_{OM}, \quad (B8)$$

where $\gamma = \gamma_0 + \gamma_b$ is the total decay rate of the mechanical mode, with γ_0 the coupling to the millikelvin fridge bath. The driving term includes the steady-state occupation n_b of the laser-induced thermal bath, the fraction δ of the hot thermal bath that is slow to turn on, and the turn-on rate γ_s of the hot bath. When the optical pump is turned off, the transducer will cool down towards the ground state at rate γ_0 [82].

1. State-of-the-art-transducer design

In this section, we benchmark the performance of microwave-optical Bell-state production in our scheme using the transducer design from Ref. [66]. We do not assume that we have access to superconducting qubits

that preserve their coherence in the presence of an optical pulse, but we assume that the qubits in our architecture have recovery times on the order of 10 ns, or that the qubits are shielded from the stray optical photons coming from the pump. Achieving proper shielding and fast recovery of the superconducting qubit under optical illumination is an active research area where significant progress is being made by the use of gap engineering and low-quasiparticle-lifetime materials. An overview of the performance parameters of the state-of-the-art transducers used in our simulation is shown in Table I.

We use Eq. (B8) to estimate the expected number of thermal phonons in the mechanical mode after the pump pulse. The transducer cannot be squeezed very hard because of the strong external coupling to the optical
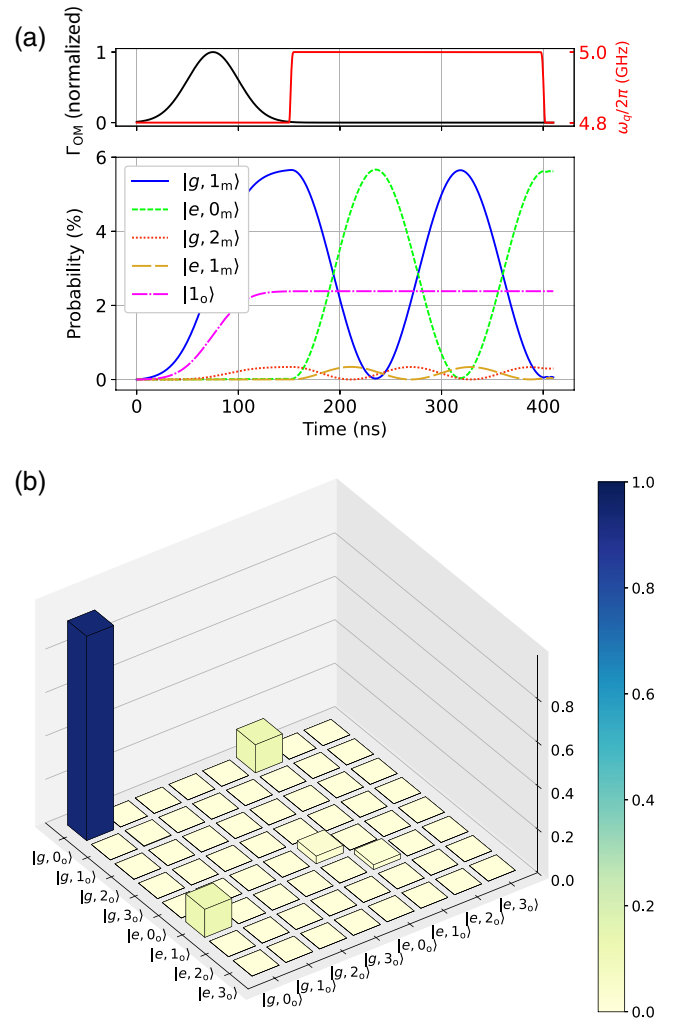

FIG. 9. Simulation results obtained with the state-of-the-art-transducer design parameters in Table I. (a) Evolution of the probabilities of finding the transducer system in the state $|n_q n_m\rangle$. The probability of finding an optical photon in the virtual cavity representing the output waveguide is also shown. (b) Reduced density matrix of the transmon qubit and the optical output from the transducer at the end of the simulation.

cavity. This limits the number of down-converted phonons, and so $\langle n \rangle \lesssim 0.05$. We find that, during the pump pulse, the peak optomechanical scattering rate is 540 kHz, and so the first term on the right-hand side of Eq. (B8) is less than $\lesssim 27$ KHz. The second term is much larger, since $\gamma_b n_b \sim 2\pi \times 100$ KHz. The third term is just the optomechanical scattering rate, which we found to be similar to $\gamma_b n_b$. Dropping the first term and integrating Eq. (B8), we find that for a square pulse of duration 50 ns (similar in length to the Gaussian pulse in the simulation), the number of phonons should be approximately 0.03. This is consistent with the estimate of 0.5 added noise phonons for a pulse of 500 ns from Ref. [66]. The number of phonons in the mechanical mode originating from the spontaneous down-conversion process is here expected to be similar to the number of thermal phonons.

We now simulate the transducer described above using the QuTiP package [79] with each mode in Fig. 8 having a four-dimensional Hilbert space. The probability of finding the superconducting qubit and the mechanical mode in the state $|n_q n_m\rangle$, where $0_q = g$ and $1_q = e$, is given by

$$P_{n_q n_m}(t) = \langle n_q n_m | \hat{\rho}_{qm}(t) | n_q n_m \rangle, \tag{B9}$$

where $\hat{\rho}_{qm}(t) = \text{Tr}_{c,d}\left[\hat{\rho}(t)\right]$ is the state of the superconducting qubit and the mechanical mode after we have traced out the optical cavity and virtual-cavity modes. Starting from the vacuum state $\hat{\rho}_{qm}(0) = |\text{vac}\rangle\langle\text{vac}|$, the evolution of $P_{n_q n_m}$ under Eq. (B3) is shown in Fig. 9(a). We have included only the relevant states for our scheme; vacuum is the dominant contribution to $\hat{\rho}_{qm}$, but does not play a role in our scheme, while states with more than two excitations have vanishing contributions. We recognize the expected behavior of the mechanical mode during squeezing, where $P_{02} \approx (P_{01})^2$. We have also included the probability of finding one photon in the virtual-cavity

mode, which represents the optical output from the transducer. The simulated probabilities validate our estimate of the thermal-phonon contribution to the final transmon population, although the heating appears to be around the upper end of the estimate. This can be attributed mainly to the use of a Gaussian pulse shape in the simulation, which implies that the optical pump is heating the transducer for a longer period than in our crude estimate with a square pulse. We see from Fig. 9 that the probability of finding an optical photon in a wave packet emitted from the transducer is roughly 40% when the transmon is in the first excited state. We know that $\kappa_{int}/(\kappa_{ex} + \kappa_{int}) = 29\%$ of optical photons are lost to intrinsic loss channels in the transducer. The remaining observed loss is mainly due to thermal phonons populating the transducer's mechanical mode while the laser is switched on. Heating of the transmon qubit from the microwave-photon bath is negligible on the timescale of the simulation.

We are also interested in the coherence of the microwave-optical state that will be used to form one rail in a microwave-optical dual-rail Bell pair. The reduced density matrix of the transmon qubit and the virtual cavity representing the outgoing optical wave packet is shown in Fig. 9(b). To estimate the fidelity of a heralded Bell pair, we take two copies of the reduced density matrix in Fig. 9(b) and form the density matrix $\hat{\rho}_{DR} = \hat{\rho}_{R1} \otimes \hat{\rho}_{R2}$. The heralding projects this state onto the subspace where either of the two transmons is excited. Specifically, we take the heralding operation to measure the observable associated with the operator $\hat{Z}_{q1}\hat{Z}_{q2}$ [74]. We express the eigenspace of this operator in a tensor product with the identity operator applied to the optical output from the transducer using a basis that includes the target dual-rail microwave-optical state $|+\rangle_H = (|0_e\rangle|0_o\rangle + |1_e\rangle|1_o\rangle)/\sqrt{2}$. This allows us to express the postheralding density matrix as

$$\hat{\rho} = \frac{1}{P(n_{q,R1} + n_{q,R2} = 1)}\left[P_{|+\rangle_H}|+\rangle_H\langle+| + \frac{1}{2}\sum_{n \neq 1} P_{n,+}\left(|0_{q1}0_{o1}1_{q2}n_{o2}\rangle + |1_{q1}n_{o1}0_{q2}0_{o2}\rangle\right)\left(\langle 0_{q1}0_{o1}1_{q2}n_{o2}| + \langle 1_{q1}n_{o1}0_{q2}0_{o2}|\right) \right.$$

$$\left. + \frac{1}{2}\sum_{n \neq 1} P_{n,-}\left(|0_{q1}0_{o1}1_{q2}n_{o2}\rangle - |1_{q1}n_{o1}0_{q2}0_{o2}\rangle\right)\left(\langle 0_{q1}0_{o1}1_{q2}n_{o2}| - \langle 1_{q1}n_{o1}0_{q2}0_{o2}|\right) + \dots \right]. \tag{B10}$$

The first and second sums in Eq. (B10) capture cases where the transmon qubit is excited but the number of photons in the corresponding optical output mode is more

than 1 or zero—representing multiphoton noise and photon loss, respectively. Here, $P(n_{q,R1} + n_{q,R2} = 1)$ is the total probability that a perfect measurement of $\hat{Z}_{q,R1}\hat{Z}_{q,R2}$ returns

TABLE III. Overlaps of the simulated state produced from a single block in our scheme with selected candidate states before and after heralding. Before heralding the overlap with the vacuum state is dominant, as can be seen in Fig. 9(b).

State	Before heralding	After heralding	Error observed
$|+\rangle_H$	0.041	0.380	
$\left(|0_{q1}0_{o1}1_{q2}0_{o2}\rangle \pm |1_{q1}0_{o1}0_{q2}0_{o2}\rangle\right)/\sqrt{2}$	0.066	0.614	Photon loss
$\left(|0_{q1}0_{o1}1_{q2}2_{o2}\rangle \pm |1_{q1}2_{o1}0_{q2}0_{o2}\rangle\right)/\sqrt{2}$	<0.001	0.003	Multiphoton noise

-1. The probability of finding a microwave-optical dual-rail Bell pair $|+\rangle_H$ is shown in Table III along with the most likely other states.

The low fidelity of 38% is mainly due to the high coupling of the optical cavity in the transducer to intrinsic loss channels and thermal noise. If we ignore finite phonon-photon swap efficiency and multiphoton noise for a moment, the "signal-to-noise" (SNR) ratio in the heralding process is given approximately by $\Gamma_{OM}\tau_{pulse}\eta_o/n_{th}$, where $\eta_o = \kappa_{ex}/\kappa$ is the optical photon extraction efficiency and n_{th} is the number of thermal phonons in the mechanical mode of the transducer. Since $\Gamma_{OM} \propto \kappa^{-1}$, we see that the SNR is proportional to κ^{-2}. An increase in the optical quality factor of the transducer would therefore lead to markedly greater fidelity of the microwave-optical Bell pair. Indeed, the optical quality factor in piezo-optomechanical transducers is the most important area of improvement for practical use of our scheme. Remarkably, the theoretical threshold for photon loss in fault-tolerant linear optical quantum computation is 50% [83]. The simulated device is thus closer to being compatible with fault-tolerant quantum computation than what might be believed from the low fidelity alone—although the overhead required would be completely impractical with photon loss rates of around 50%. Of course, there are several other challenges that are not captured by the simulation here, including high-fidelity heralding, microwave processing after heralding, and distinguishable optical photons coming from different devices.

2. Improved transducers

In Sec. IV, we argue that our scheme can produce resource states from microwave-optical Bell pairs at the threshold for fault-tolerant fusion-based or measurement-based quantum computation. Here we simulate the preparation of a microwave-optical Bell state using transducers that have better performance for three key parameters: intrinsic optical quality factor, mechanical mode heating, and electromechanical coupling. Although the precise mechanism for mechanical mode heating in optomechanical crystals is still under investigation, there is reason to believe that higher intrinsic optical quality factors will reduce the sources of mechanical heating as well. Moreover, a quasi-2D optomechanical crystal with a hot-phonon-bath population n_b reduced by more than a factor

of 7 compared with the conventional nanobeam design was recently demonstrated [81]. We do not want to understate the challenge in making transducers with this kind of performance, but such demonstrations indicate that a fundamental redesign of transducers in order to match the parameters used in our simulations is not necessary.

We rerun the simulation described in Appendix B 1 with updated parameters for transducer and qubit performance as shown in Table I. In addition to decreasing the intrinsic loss of the optical cavity, we have also increased the mechanical mode's loss to the fridge bath by a factor of 10. Ultrahigh mechanical quality factors, such as those demonstrated in optomechanical crystals [59,81], are not necessary for our scheme provided the electromechanical coupling is sufficiently strong. Low mechanical loss rates reduce the repetition rate of our scheme, which is undesirable for resource-intensive, long-term applications such as quantum communication and (especially) quantum computation. The density matrices at the end of each simulation are shown in Fig. 10. Each mode was simulated with a four-dimensional Hilbert space. The squeezing is so strong that it introduces significant components of the two-photon and three-photon states that can lead to multiphoton noise. Four-photon contributions are not captured by the simulation, but will only marginally alter the results. Increasing the dimensions of the Hilbert space of the modes is computationally demanding, and the additional accuracy does not reflect the uncertainty in the parameters for the transducer in the simulation. Comparing this result with the result in Fig. 9(b), we see that a larger share of the total contribution to the density matrix comes from the state $|e, 1_o\rangle$. This increase in SNR confirms the importance of reducing the intrinsic optical loss of the transducer. However, the strong squeezing leads to undesirable populations along the diagonal of the density matrix, which in turn lead to multiphoton noise in the heralded microwave-optical Bell pair. The simulation shows that most heralding events correspond to a true microwave-optical Bell pair. The dominant error source is optical photon loss, either from thermal phonons being swapped to the qubit or from scattered photons being lost to one of the intrinsic loss channels in the optical cavity of the transducer. However, the strong squeezing produces a significant amount of multiphoton noise as well. The swap time was not optimized to reduce multiphoton noise in this simulation.
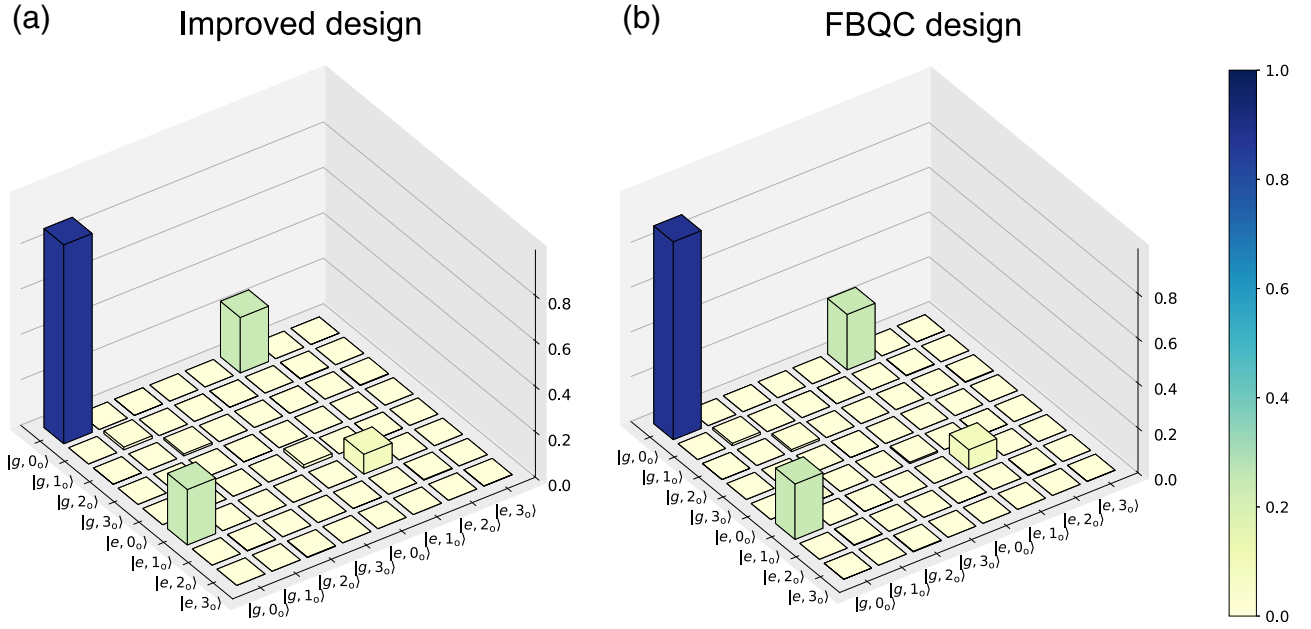
FIG. 10.   Density matrices for one rail after the swap operation from the transducer to the transmon qubit using the two transducers in Table I with improved performance: (a) improved design; (b) FBQC design.

APPENDIX C: ERROR PROCESSES

In this appendix, we present a more detailed description of error processes in the hardware and their effects on resource states. Analyses and measurements of error rates of dual-rail qubits and cavities have been performed elsewhere [38–40,98]. Many of the results obtained apply to the superconducting architecture of our scheme. The scheme could be adapted to cavities instead of transmon qubits forming the rails. However, the requirements for microwave dual-rail qubits in our scheme are less demanding than they are for dual-rail qubits used in direct processing of quantum information, since leakage in the microwave dual-rail qubit will be detected when we measure the state of the qubits. Should our measurements indicate that leakage has occurred, we may erase all affected qubits before they are used in a computation on a photonic quantum processor. Errors in the heralding process could lead to multiphoton noise in the optical qubits, but this will not lead to logical errors in the computation. Such leakage will be detected when the optical qubits are fused or measured, as long as the error rate is below the thresholds for fault tolerance in fusion-based or measurement-based computational schemes [12,41,99].

In Sec. IV, we explain the first-order error mechanisms in our scheme and their effect on the resource states. We focus primarily on the matter-based parts of our scheme (i.e., the mechanical mode and the microwave dual-rail qubit) because we expect the optical side to be dominated by photon loss. The optical photons will not be completely indistinguishable due to disorder, which leads to errors when the photons are interfered. Such disorder in the optical and mechanical frequencies may be addressed through, for example, frequency shifting [100] or tuning.

We summarize the expected error sources and their contribution to errors in the optical output of the resource states in Table IV. We expect that a low efficiency of extraction from the optical cavities will result in photon loss rates on the order of 10%. Pump photons will have to be filtered out from the optical output, which will further increase the photon loss rate. Further, for the mechanical mode and the superconducting qubits, there are several sources of errors with various degrees of severity. Thermal noise in the mechanical mode will primarily contribute to false heralding of a Bell pair, which is equivalent to a correctly heralded Bell pair with its optical photon missing. Thermal phonons may appear in the mechanical mode while the Bell pair is being prepared, or the mechanical mode might not be fully in its ground state at the beginning of a clock cycle. The latter could be the dominant contribution, particularly when the resource-state generator is operated at high rates.

When we pump the optomechanical crystal to produce phonon-photon pairs, there is a risk of producing more than one such pair from the same pump pulse. As is evident from the simulations presented in Appendix B, this will lead to multiphoton noise in the optical qubits. We propose suppressing this noise by using the mechanics-qubit swap to avoid heralding from two-phonon states. While the swap time can be optimized to suppress noise, it is challenging to eliminate noise from both two-phonon and

TABLE IV. Estimated error sources and effect on optical qubits in the resource states. The values given are order-of-magnitude estimates after heralding and depend on architecture, hardware performance, and the speed of qubit gates and measurements. See the simulation results presented in Appendix B for two concrete examples covering just the Bell-state preparation and heralding. We discuss only first-order effects; chains of errors that produce erasure could combine into Pauli errors, but such chains individually are unlikely to occur. Here t is the execution time of one clock cycle, t_{swap} is the swap time from the mechanical mode to the superconducting qubit, γ is the total mechanical decay rate, $T_{\phi,\text{m}}$ is the effective mechanical dephasing rate, $T_{\phi,\text{DR}}$ is the dual-rail qubit dephasing time, $T_{1,\text{DR}}$ is the dual-rail qubit T_1, η_{PC} is the parity-check fidelity, and η_{RO} is the readout fidelity for a single superconducting qubit. All other parameters are as defined before.

Error source	Effect	Scaling	Value (%)	Error type
Photon extraction	Photon loss	$\kappa_{\text{int}}/(\kappa_{\text{ex}} + \kappa_{\text{int}})$	10	Erasure
Thermal noise	False heralding	$n_{\text{b}}\gamma_{\text{b}}\left(\tau + t_{\text{swap}}\right)$	10	Erasure
Hard squeezing	Multiphoton noise	$(\Gamma_{\text{OM}}\tau)^2$	1	Leakage
Phonon loss	Multiphoton noise	$\gamma\left(\tau + t_{\text{swap}}\right)$	1	Leakage
Imperfect parity check	False heralding	$1 - \eta_{\text{PC}}$	1	Erasure
Measurement infidelity	Inconsistent measurement	$1 - \eta_{\text{RO}}$	1	Erasure
Mechanical dephasing	Phase flip	$\left(\tau + t_{\text{swap}}\right)/T_{\phi,\text{m}}$	1	Pauli error
Qubit dephasing	Phase flip	$t/T_{\phi,\text{DR}}$	0.1	Pauli error
Qubit swap	Bit flip	$t/T_{1,\text{DR}}$	0.1	Pauli error
Measurement infidelity	Phase/bit flip	$(1 - \eta_{\text{RO}})^2$	0.01	Pauli error

three-phonon states simultaneously. Assuming the optimal strategy would be to eliminate noise from two-phonon states because these are much more likely to be produced, we can estimate the level of three-photon noise from three down-converted pairs. For simplicity, we take the optomechanical crystal after the pump pulse to be in a perfect two-mode squeezed vacuum state,

$$|\psi\rangle = \sqrt{p_0}|0_{\text{m}}0_{\text{o}}\rangle + \sqrt{p_1}|1_{\text{m}}1_{\text{o}}\rangle + \sqrt{p_2}|2_{\text{m}}2_{\text{o}}\rangle$$
$$+ \sqrt{p_3}|3_{\text{m}}3_{\text{o}}\rangle + \cdots, \tag{C1}$$

where p_n is the probability of finding n phonon-photon pairs. We ignore states with four or more such pairs. From Eq. (3), it follows that $p_n = p_0(1 - p_0)^n$. Next, we count the different combinations of states that will herald a Bell pair. Our heralding scheme cannot distinguish one-phonon states from three-phonon states, nor can it distinguish two-phonon states from zero-phonon states. Combining the optomechanical transducers from both rails, we have

$$|\psi_{\text{DR}}\rangle = p_0|0_{\text{R1}}0_{\text{R2}}\rangle + \sqrt{p_0 p_1}|1_{\text{R1}}0_{\text{R2}}\rangle + \sqrt{p_0 p_1}|0_{\text{R1}}1_{\text{R2}}\rangle + \cdots$$
$$+ \sqrt{p_0 p_3}|0_{\text{R1}}3_{\text{R2}}\rangle + \sqrt{p_0 p_3}|3_{\text{R1}}0_{\text{R2}}\rangle + \sqrt{p_1 p_2}|1_{\text{R1}}2_{\text{R2}}\rangle + \sqrt{p_1 p_2}|2_{\text{R1}}1_{\text{R2}}\rangle + \cdots, \tag{C2}$$

where $|n_{\text{R1}}m_{\text{R2}}\rangle$ is the state with n phonon-photon pairs in rail 1 and m phonon-photon pairs in rail 2. We write explicitly only the terms with $n + m = 0, 1, 3$. States with $n + m = 2$ are taken care of by the heralding, while states with $n + m > 3$ are ignored. Since all the terms in Eq. (C2) apart from $|0_{\text{R1}}0_{\text{R2}}\rangle$ will herald a Bell pair, we find that the probability of having three photons in the optical rails is given by

$$P_{\text{noise}} = \frac{p_0 p_3 + p_1 p_2}{p_0 p_1 + p_0 p_3 + p_1 p_2} \approx (1 - p_0)^2 \approx p_1^2. \tag{C3}$$

Following Ref. [82], we can estimate how p_1 scales with $\Gamma_{\text{OM}}\tau$ by defining the propagator $U = \exp\left[ir\left(\hat{b}(0)\hat{C}_{\text{in}} +\right.\right.$

$\left.\left.\hat{b}^{\dagger}(0)\hat{C}_{\text{in}}^{\dagger}\right)\right]$. Using

$$p_1 \approx |\langle 1_b 1_C|U|0_b 0_C\rangle|^2 \sim r^2, \tag{C4}$$

we find from expanding both sides of $\cosh(r) = e^{\Gamma_{\text{OM}}\tau/2}$ to lowest order that

$$p_1 \sim r^2 \sim \Gamma_{\text{OM}}\tau. \tag{C5}$$

Note that this holds only for low levels of squeezing. For stronger squeezing ($p_1 > 10\%$), there will be deviations from this lowest-order result.

Phonon loss can also contribute to multiphoton noise in the optical qubits by converting a two-phonon state into a

one-phonon state, which will herald a Bell pair in the parity check. This is technically a second-order effect, because p_2 is small compared with p_1 and phonons should be quickly swapped to the superconducting qubits, but for hard pumping ($p_1 \sim 10\%$) and lossy mechanics ($\gamma/2\pi \sim 500\,\text{kHz}$), this could lead to multiphoton noise and therefore leakage rates on the order of 1%.

Infidelity in the parity check will predominantly result in an even parity being mistaken for an odd parity. The probability of such events will depend on how the parity check is implemented, but we assume a false-positive rate of order 1% is readily achievable with, for example, the readout architecture in Fig. 3. We are overwhelmingly likely to catch parity-check errors when the dual-rail qubit is measured. If a measurement of the two superconducting qubits forming the microwave dual-rail qubit indicates that a microwave photon is missing (or there is a microwave photon in each superconducting qubit), we erase this dual-rail qubit (and its entangled optical dual-rail qubit) from the resource state.

A related error source is the measurement of the superconducting qubit in each rail, which will have some fidelity η_{RO}. Because we measure each rail independently, the probability of both measurements yielding the wrong answer is $(1 - \eta_{\text{RO}})^2$, which will lead to a Pauli error. If only one measurement yields the wrong result, then the two measurements will not correspond to a valid dual-rail qubit state, and we therefore erase the qubit from the resource state. Qubit readout is an essential part of any superconducting processor, and error rates are already below 1% in state-of-the-art processors with transmon qubits [101].

Among the mechanisms we have considered so far, we believe that the primary source of Pauli errors will be dephasing of the mechanical mode before the phonon can be swapped to the superconducting qubit. Investigations into how dephasing times in the mechanical mode can be extended are encouraged. However, the relatively low phonon number in our scheme implies that the mechanical dephasing effect is reduced compared with the single-phonon dephasing rate γ_ϕ. As an illustration, consider a mechanical mode that is subject to frequency fluctuations. In a frame rotating at the mechanical frequency, the mechanical mode can be described by the master equation

$$\frac{d\hat{\rho}}{dt} = \mathcal{D}\left[\sqrt{\gamma_\phi}\hat{b}^\dagger\hat{b}\right]\hat{\rho}. \tag{C6}$$

Suppose the resonator at time t_0 is in the pure state $\hat{\rho} = \left(\sqrt{p_0}|0\rangle + \sqrt{p_1}|1\rangle\right)\left(\sqrt{p_0}\langle 0| + \sqrt{p_1}\langle 1|\right)$. In this case, Eq. (C6) becomes

$$\frac{d\rho}{dt} = -\frac{\gamma_\phi}{2}\sqrt{p_0 p_1}\left(|0\rangle\langle 1| + |1\rangle\langle 0|\right). \tag{C7}$$

This describes exponential decay of the off-diagonal terms in the density matrix at a rate that depends on the excited-state population p_1. In our protocol, $p_0 p_1 \leq 0.1$, and therefore the effective dephasing rate is smaller by at least a factor 2 than in cases where the mechanical oscillator is used as a (single-rail) qubit. Higher levels of optomechanical squeezing cause more rapid dephasing, and there might be additional, second-order processes that can lead to dephasing in the strong-squeezing case simulated in Appendix B 2. For example, we suspect that optical photon loss ($\lesssim 10\%$) combined with thermal noise and multiphoton noise (which can add up to $\sim 10\%$) could have a similar contribution to the simulated phase flip rate.

After the phonon-photon swap operation, there will be dephasing of the microwave dual-rail qubit before it is measured. Promising investigations into such dephasing began recently [40]. To minimize such errors, we should minimize the time from Bell-state preparation until the microwave dual-rail qubits are measured and maximize T_ϕ for the dual-rail qubit. The time from start to end of a single clock cycle as described in Sec. III will be similar to a surface-code cycle [102], which is likely to be around 1 µs. With single-transmon dephasing times up to 100 µs [103,104], dual-rail T_ϕ on the order of 10 ms should be possible [39]. We expect that Pauli error from decoherence of the superconducting dual-rail qubit can thus be kept well below the threshold for fault tolerance.

APPENDIX D: TWO-QUBIT GATES BETWEEN HYBRID QUBITS

We define hybrid qubits in Sec. III with a repetition code using the microwave and optical dual-rail qubits. Specifically, our protocol prepares the hybrid states

$$|+\rangle_{\text{H}} = \frac{1}{\sqrt{2}}\left(|0_{\text{e}}\rangle|0_{\text{o}}\rangle + |1_{\text{e}}\rangle|1_{\text{o}}\rangle\right), \tag{D1}$$

where the dual-rail qubits are encoded as ($i = \text{e, o}$)

$$|0_i\rangle = \frac{1}{\sqrt{2}}\left(|0_i\rangle_{\text{R1}}|1_i\rangle_{\text{R2}} + |1_i\rangle_{\text{R1}}|0_i\rangle_{\text{R2}}\right), \tag{D2}$$

$$|1_i\rangle = \frac{1}{\sqrt{2}}\left(|0_i\rangle_{\text{R1}}|1_i\rangle_{\text{R2}} - |1_i\rangle_{\text{R1}}|0_i\rangle_{\text{R2}}\right) \tag{D3}$$

when expressed as the Fock state of the rails R1 and R2 in the microwave domain (e) and the optical domain (o). Building graph states requires that we apply CZ gates between microwave qubits belonging to different hybrid states $|+\rangle_{\text{H}}$. This can be done in a straightforward way by bringing the state $|1_{\text{e}}\rangle|1_{\text{e}}\rangle$ into resonance with a noncomputational state [105]. While the phase between two dual-rail qubits could be affected while idling at the avoided crossing, this can be corrected with single-qubit gates [63]. We expect that CZ gates applied in this way may achieve

greater fidelities than transmon-transmon CZ gates due to the dual-rail qubits' protection from dephasing [40,63].

Alternatively, we may implement CZ gates from $\sqrt{i\text{SWAP}}$ gates between dual-rail qubits and single-qubit gates. For example, we can adiabatically turn on the interaction g_c between two transmons from different blocks to realize the effective Hamiltonian [39]

$$\hat{H}_{\text{eff}} = \frac{\Omega}{2}\left(\hat{\sigma}_1^z + \hat{\sigma}_2^z\right) + g_{XX}\hat{\sigma}_1^x\hat{\sigma}_2^x, \qquad (D4)$$

where $\Omega = 2g_{12}\left(1 + 6g_c^2/\Delta^2\right)$ and $g_{XX} = -4g_c^2 E_C/\left(\Delta^2 - E_C^2\right)$ when the transmons within each block are on

resonance and coupled at rate g_c, but transmons from different blocks are detuned by Δ. The Pauli matrices $\hat{\sigma}_i^z, \hat{\sigma}_i^x$ generate rotations of the dual-rail qubits $i = 1,2$ around the z axis and the x axis, respectively. After a time T such that $\int_0^T g_{XX}(t)dt = \pi/4$, $\hat{H}_{\text{eff}}$ has implemented the gate $\sqrt{i\text{SWAP}}\exp\left[-i\phi\left(\hat{\sigma}_1^z + \hat{\sigma}_2^z\right)\right]$, where $\phi = \int_0^T \sqrt{\Omega^2 + g_{XX}^2}\,dt$ [39]. If we apply gates to the microwave dual-rail qubit in each hybrid qubit, the following circuit then implements the CZ gate on two hybrid qubits:
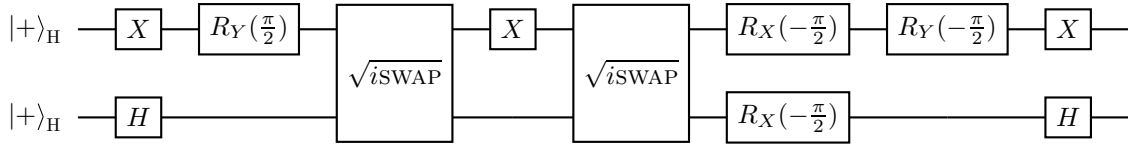
APPENDIX E: TURNING ON THE TRANSMON-TRANSMON COUPLING

After the parity check in our protocol (see Sec. III), we have the state $|+\rangle_{\text{H}} = \frac{1}{\sqrt{2}}\left(|0_e\rangle|0_o\rangle + |1_e\rangle|1_o\rangle\right)$. The $|0_e\rangle$ and $|1_e\rangle$ states lose their degeneracy as we turn on the transmon-transmon coupling. In addition, $|+\rangle_{\text{H}}$ is not an eigenstate of the Hamiltonian governing the system. An ideal coupler would allow us to realize a Hamiltonian where there are no transitions between the states $|0_e\rangle$ and $|1_e\rangle$, nor between any computational and noncomputational state, thus allowing us to tune the coupling strength arbitrarily fast (confirmed through a QuTiP simulation [79]). However, tunable couplers are multilevel systems where unwanted transitions can occur. This implies that calibration is necessary to find an optimal tuning speed that maximizes fidelity [106].

[1] R. Horodecki, P. Horodecki, M. Horodecki, and K. Horodecki, Quantum entanglement, Rev. Mod. Phys. **81**, 865 (2009).

[2] A. Blais, A. L. Grimsmo, S. Girvin, and A. Wallraff, Circuit quantum electrodynamics, Rev. Mod. Phys. **93**, 025005 (2021).

[3] X. Gu, A. F. Kockum, A. Miranowicz, Y.-X. Liu, and F. Nori, Microwave photonics with superconducting quantum circuits, Phys. Rep. **718–719**, 1 (2017).

[4] W. Asavanant, Y. Shiozawa, S. Yokoyama, B. Charoensombutamon, H. Emura, R. N. Alexander, S. Takeda, J.-I. Yoshikawa, N. C. Menicucci, H. Yonezawa, and A. Furusawa, Generation of time-domain-multiplexed two-dimensional cluster state, Science **366**, 373 (2019).

[5] M. V. Larsen, X. Guo, C. R. Breum, J. S. Neergaard-Nielsen, and U. L. Andersen, Deterministic generation of a two-dimensional cluster state, Science **366**, 369 (2019).

[6] D. Leibfried, R. Blatt, C. Monroe, and D. Wineland, Quantum dynamics of single trapped ions, Rev. Mod. Phys. **75**, 281 (2003).

[7] J. Benhelm, G. Kirchmair, C. F. Roos, and R. Blatt, Towards fault-tolerant quantum computing with trapped ions, Nat. Phys. **4**, 463 (2008).

[8] C. D. Bruzewicz, J. Chiaverini, R. McConnell, and J. M. Sage, Trapped-ion quantum computing: Progress and challenges, Appl. Phys. Rev. **6**, 021314 (2019).

[9] P. Kok, W. J. Munro, K. Nemoto, T. C. Ralph, J. P. Dowling, and G. J. Milburn, Linear optical quantum computing with photonic qubits, Rev. Mod. Phys. **79**, 135 (2007).

[10] D. E. Browne and T. Rudolph, Resource-efficient linear optical quantum computation, Phys. Rev. Lett. **95**, 010501 (2005).

[11] M. Varnava, D. E. Browne, and T. Rudolph, How good must single photon sources and detectors be for efficient linear optical quantum computation?, Phys. Rev. Lett. **100**, 060502 (2008).

[12] S. Bartolucci, P. Birchall, H. Bombín, H. Cable, C. Dawson, M. Gimeno-Segovia, E. Johnston, K. Kieling, N. Nickerson, M. Pant, F. Pastawski, T. Rudolph, and C. Sparrow, Fusion-based quantum computation, Nat. Commun. **14**, 912 (2023).

[13] J. Zhao, C. Ma, M. Rüsing, and S. Mookherjea, High quality entangled photon pair generation in periodically poled thin-film lithium niobate waveguides, Phys. Rev. Lett. **124**, 163603 (2020).

[14] Z. Zhang, C. Yuan, S. Shen, H. Yu, R. Zhang, H. Wang, H. Li, Y. Wang, G. Deng, Z. Wang, L. You, Z. Wang, H. Song, G. Guo, and Q. Zhou, High-performance quantum entanglement generation via cascaded second-order nonlinear processes, npj Quantum Inf. **7,** 123 (2021).

[15] M. Cabrejo-Ponce, C. Spiess, A. L. Marques Muniz, P. Ancsin, and F. Steinlechner, GHz-pulsed source of entangled photons for reconfigurable quantum networks, Quantum Sci. Technol. **7,** 045022 (2022).

[16] C. Ma, X. Wang, V. Anant, A. D. Beyer, M. D. Shaw, and S. Mookherjea, Silicon photonic entangled photon-pair and heralded single photon generation with CAR > 12 000 and $g^{(2)}(0) < 0.006$, Opt. Express **25,** 32995 (2017).

[17] S. Paesani, M. Borghi, S. Signorini, A. Maïnos, L. Pavesi, and A. Laing, Near-ideal spontaneous photon sources in silicon quantum photonics, Nat. Commun. **11,** 2505 (2020).

[18] T. J. Steiner, J. E. Castro, L. Chang, Q. Dang, W. Xie, J. Norman, J. E. Bowers, and G. Moody, Ultrabright entangled-photon-pair generation from an AlGaAs-on-insulator microring resonator, PRX Quantum **2,** 010337 (2021).

[19] N. H. Lindner and T. Rudolph, Proposal for pulsed on-demand sources of photonic cluster state strings, Phys. Rev. Lett. **103,** 113602 (2009).

[20] S. E. Economou, N. Lindner, and T. Rudolph, Optically generated 2-dimensional photonic cluster state from coupled quantum dots, Phys. Rev. Lett. **105,** 093601 (2010).

[21] I. Schwartz, D. Cogan, E. R. Schmidgall, Y. Don, L. Gantz, O. Kenneth, N. H. Lindner, and D. Gershoni, Deterministic generation of a cluster state of entangled photons, Science **354,** 434 (2016).

[22] R. Uppu, L. Midolo, X. Zhou, J. Carolan, and P. Lodahl, Quantum-dot-based deterministic photon–emitter interfaces for scalable photonic quantum technology, Nat. Nanotechnol. **16,** 1308 (2021).

[23] D. Cogan, Z.-E. Su, O. Kenneth, and D. Gershoni, Deterministic generation of indistinguishable photons in a cluster state, Nat. Photonics **17,** 324 (2023).

[24] H. Cao, L. M. Hansen, F. Giorgino, L. Carosini, P. Zahálka, F. Zilk, J. C. Loredo, and P. Walther, Photonic source of heralded Greenberger-Horne-Zeilinger states, Phys. Rev. Lett. **132,** 130604 (2024).

[25] S. Chen, L.-C. Peng, Y.-P. Guo, X.-M. Gu, X. Ding, R.-Z. Liu, J.-Y. Zhao, X. You, J. Qin, Y.-F. Wang, Y.-M. He, J. J. Renema, Y.-H. Huo, H. Wang, C.-Y. Lu, and J.-W. Pan, Heralded three-photon entanglement from a single-photon source on a photonic chip, Phys. Rev. Lett. **132,** 130603 (2024).

[26] Y.-D. Wang and A. A. Clerk, Using dark modes for high-fidelity optomechanical quantum state transfer, New J. Phys. **14,** 105010 (2012).

[27] C. Zhong, X. Han, and L. Jiang, Microwave and optical entanglement for quantum transduction with electro-optomechanics, Phys. Rev. Appl. **18,** 054061 (2022).

[28] W. Jiang, C. J. Sarabalis, Y. D. Dahmani, R. N. Patel, F. M. Mayor, T. P. McKenna, R. Van Laer, and A. H. Safavi-Naeini, Efficient bidirectional piezo-optomechanical transduction between microwave and optical frequency, Nat. Commun. **11,** 1166 (2020).

[29] M. Mirhosseini, A. Sipahigil, M. Kalaee, and O. Painter, Superconducting qubit to optical photon transduction, Nature **588,** 599 (2020).

[30] W. Jiang, F. M. Mayor, S. Malik, R. Van Laer, T. P. McKenna, R. N. Patel, J. D. Witmer, and A. H. Safavi-Naeini, Optically heralded microwave photon addition, Nat. Phys. **19,** 1423 (2023).

[31] M. J. Weaver, P. Duivestein, A. C. Bernasconi, S. Scharmer, M. Lemang, T. C. v. Thiel, F. Hijazi, B. Hensen, S. Gröblacher, and R. Stockill, An integrated microwave-to-optics interface for scalable quantum computing, Nat. Nanotechnol. **19,** 166 (2023).

[32] R. Sahu, L. Qiu, W. Hease, G. Arnold, Y. Minoguchi, P. Rabl, and J. M. Fink, Entangling microwaves with light, Science **380,** 718 (2023).

[33] S. Meesala, S. Wood, D. Lake, P. Chiappina, C. Zhong, A. D. Beyer, M. D. Shaw, L. Jiang, and O. Painter, Nonclassical microwave–optical photon pair generation with a chip-scale transducer, Nat. Phys. **20,** 871 (2024).

[34] C. Zhong, Z. Wang, C. Zou, M. Zhang, X. Han, W. Fu, M. Xu, S. Shankar, M. H. Devoret, H. X. Tang, and L. Jiang, Proposal for heralded generation and detection of entangled microwave–optical-photon pairs, Phys. Rev. Lett. **124,** 010511 (2020).

[35] C. Zhong, X. Han, H. X. Tang, and L. Jiang, Entanglement of microwave-optical modes in a strongly coupled electro-optomechanical system, Phys. Rev. A **101,** 032345 (2020).

[36] K. Azuma, K. Tamaki, and H.-K. Lo, All-photonic quantum repeaters, Nat. Commun. **6,** 6787 (2015).

[37] H. Bombin, I. H. Kim, D. Litinski, N. Nickerson, M. Pant, F. Pastawski, S. Roberts, and T. Rudolph, Interleaving: Modular architectures for fault-tolerant photonic quantum computing, ArXiv:2103.08612.

[38] J. D. Teoh, P. Winkel, H. K. Babla, B. J. Chapman, J. Claes, S. J. de Graaf, J. W. O. Garmon, W. D. Kalfus, Y. Lu, A. Maiti, K. Sahay, N. Thakur, T. Tsunoda, S. H. Xue, L. Frunzio, S. M. Girvin, S. Puri, and R. J. Schoelkopf, Dual-rail encoding with superconducting cavities, Proc. Natl. Acad. Sci. **120,** e2221736120 (2023).

[39] A. Kubica, A. Haim, Y. Vaknin, H. Levine, F. Brandão, and A. Retzker, Erasure qubits: Overcoming the T_1 limit in superconducting circuits, Phys. Rev. X **13,** 041022 (2023).

[40] H. Levine, *et al.*, Demonstrating a long-coherence dual-rail erasure qubit using tunable transmons, Phys. Rev. X **14,** 011051 (2024).

[41] T. J. Bell, L. A. Pettersson, and S. Paesani, Optimizing graph codes for measurement-based loss tolerance, PRX Quantum **4,** 020328 (2023).

[42] H. Bombin, C. Dawson, T. Farrelly, Y. Liu, N. Nickerson, M. Pant, F. Pastawski, and S. Roberts, Fault-tolerant complexes, ArXiv:2308.07844.

[43] S. Krastanov, H. Raniwala, J. Holzgrafe, K. Jacobs, M. Lončar, M. J. Reagor, and D. R. Englund, Optically heralded entanglement of superconducting systems in quantum networks, Phys. Rev. Lett. **127,** 040503 (2021).

[44] L. M. Duan, M. D. Lukin, J. I. Cirac, and P. Zoller, Long-distance quantum communication with atomic ensembles and linear optics, Nature **414,** 413 (2001).

[45] C. D. Wilen, S. Abdullah, N. A. Kurinsky, C. Stanford, L. Cardani, G. D'Imperio, C. Tomei, L. Faoro, L. B. Ioffe, C. H. Liu, A. Opremcak, B. G. Christensen, J. L. DuBois, and R. McDermott, Correlated charge noise and relaxation errors in superconducting qubits, Nature **594,** 369 (2021).

[46] M. McEwen, *et al.*, Resolving catastrophic error bursts from cosmic rays in large arrays of superconducting qubits, Nat. Phys. **18,** 107 (2022).

[47] N. P. Breuckmann and J. N. Eberhardt, Quantum low-density parity-check codes, PRX Quantum **2,** 040101 (2021).

[48] H. Bombín, C. Dawson, R. V. Mishmash, N. Nickerson, F. Pastawski, and S. Roberts, Logical blocks for fault-tolerant topological quantum computation, PRX Quantum **4,** 020303 (2023).

[49] D. Litinski and N. Nickerson, Active volume: An architecture for efficient fault-tolerant quantum computers with limited non-local connections, ArXiv:2211.15465.

[50] A. G. Fowler, Coping with qubit leakage in topological codes, Phys. Rev. A **88,** 042308 (2013).

[51] B. M. Varbanov, F. Battistel, B. M. Tarasinski, V. P. Ostroukh, T. E. O'Brien, L. DiCarlo, and B. M. Terhal, Leakage detection for a transmon-based surface code, npj Quantum Inf. **6,** 102 (2020).

[52] R. D. Delaney, M. D. Urmey, S. Mittal, B. M. Brubaker, J. M. Kindem, P. S. Burns, C. A. Regal, and K. W. Lehnert, Superconducting-qubit readout via low-backaction electro-optic transduction, Nature **606,** 489 (2022).

[53] S. Bravyi, A. W. Cross, J. M. Gambetta, D. Maslov, P. Rall, and T. J. Yoder, High-threshold and low-overhead fault-tolerant quantum memory, Nature **627,** 778 (2024).

[54] V. S. Ferreira, G. Kim, A. Butler, H. Pichler, and O. Painter, Deterministic generation of multidimensional photonic cluster states with a single quantum emitter, Nat. Phys. **20,** 865 (2024).

[55] E. A. Wollack, A. Y. Cleland, R. G. Gruenke, Z. Wang, P. Arrangoiz-Arriola, and A. H. Safavi-Naeini, Quantum state preparation and tomography of entangled mechanical resonators, Nature **604,** 463 (2022).

[56] P. Arrangoiz-Arriola, E. A. Wollack, Z. Wang, M. Pechal, W. Jiang, T. P. McKenna, J. D. Witmer, R. Van Laer, and A. H. Safavi-Naeini, Resolving the energy levels of a nanomechanical oscillator, Nature **571,** 537 (2019).

[57] A. Bozkurt, H. Zhao, C. Joshi, H. G. LeDuc, P. K. Day, and M. Mirhosseini, A quantum electromechanical interface for long-lived phonons, Nat. Phys. **19,** 1326 (2023).

[58] J. Koch, T. M. Yu, J. Gambetta, A. A. Houck, D. I. Schuster, J. Majer, A. Blais, M. H. Devoret, S. M. Girvin, and R. J. Schoelkopf, Charge-insensitive qubit design derived from the Cooper pair box, Phys. Rev. A **76,** 042319 (2007).

[59] G. S. MacCabe, H. Ren, J. Luo, J. D. Cohen, H. Zhou, A. Sipahigil, M. Mirhosseini, and O. Painter, Nano-acoustic resonator with ultralong phonon lifetime, Science **370,** 840 (2020).

[60] F. Arute, *et al.*, Quantum supremacy using a programmable superconducting processor, Nature **574,** 505 (2019).

[61] M. Gong, *et al.*, Quantum walks on a programmable two-dimensional 62-qubit superconducting processor, Science **372,** 948 (2021).

[62] Y. Kim, A. Eddins, S. Anand, K. X. Wei, E. van den Berg, S. Rosenblatt, H. Nayfeh, Y. Wu, M. Zaletel, K. Temme, and A. Kandala, Evidence for the utility of quantum computing before fault tolerance, Nature **618,** 500 (2023).

[63] D. L. Campbell, Y.-P. Shim, B. Kannan, R. Winik, D. K. Kim, A. Melville, B. M. Niedzielski, J. L. Yoder, C. Tahan, S. Gustavsson, and W. D. Oliver, Universal nonadiabatic control of small-gap superconducting qubits, Phys. Rev. X **10,** 041051 (2020).

[64] S. Kosen, H.-X. Li, M. Rommel, R. Rehammar, M. Caputo, L. Grönberg, J. Fernández-Pendás, A. F. Kockum, J. Biznárová, L. Chen, C. Križan, A. Nylander, A. Osman, A. F. Roudsari, D. Shiri, G. Tancredi, J. Govenius, and J. Bylander, Signal crosstalk in a flip-chip quantum processor, PRX Quantum **5,** 030350 (2024).

[65] X. Han, W. Fu, C.-L. Zou, L. Jiang, and H. X. Tang, Microwave-optical quantum frequency conversion, Optica **8,** 1050 (2021).

[66] P. Chiappina, J. Banker, S. Meesala, D. Lake, S. Wood, and O. Painter, Design of an ultra-low mode volume piezo-optomechanical quantum transducer, Opt. Express **31,** 22914 (2023).

[67] Y. Zhou, Z. Zhang, Z. Yin, S. Huai, X. Gu, X. Xu, J. Allcock, F. Liu, G. Xi, Q. Yu, H. Zhang, M. Zhang, H. Li, X. Song, Z. Wang, D. Zheng, S. An, Y. Zheng, and S. Zhang, Rapid and unconditional parametric reset protocol for tunable superconducting qubits, Nat. Commun. **12,** 5924 (2021).

[68] S. G. Hofer, W. Wieczorek, M. Aspelmeyer, and K. Hammerer, Quantum entanglement and teleportation in pulsed cavity optomechanics, Phys. Rev. A **84,** 052327 (2011).

[69] M. Rol, F. Battistel, F. Malinowski, C. Bultink, B. Tarasinski, R. Vollmer, N. Haider, N. Muthusubramanian, A. Bruno, B. Terhal, and L. DiCarlo, Fast, high-fidelity conditional-phase gate exploiting leakage interference in weakly anharmonic superconducting qubits, Phys. Rev. Lett. **123,** 120502 (2019).

[70] Y. Chen, *et al.*, Qubit architecture with high coherence and fast tunable coupling, Phys. Rev. Lett. **113,** 220502 (2014).

[71] Y. Sung, L. Ding, J. Braumüller, A. Vepsäläinen, B. Kannan, M. Kjaergaard, A. Greene, G. O. Samach, C. McNally, D. Kim, A. Melville, B. M. Niedzielski, M. E. Schwartz, J. L. Yoder, T. P. Orlando, S. Gustavsson, and W. D. Oliver, Realization of high-fidelity CZ and ZZ-free iSWAP gates with a tunable coupler, Phys. Rev. X **11,** 021058 (2021).

[72] L. Tornberg and G. Johansson, High-fidelity feedback-assisted parity measurement in circuit QED, Phys. Rev. A **82,** 012329 (2010).

[73] A. Frisk Kockum, L. Tornberg, and G. Johansson, Undoing measurement-induced dephasing in circuit QED, Phys. Rev. A **85,** 052318 (2012).

[74] D. Ristè, M. Dukalski, C. A. Watson, G. De Lange, M. J. Tiggelman, Y. M. Blanter, K. W. Lehnert, R. N. Schouten,

and L. DiCarlo, Deterministic entanglement of superconducting qubits by parity measurement and feedback, Nature **502,** 350 (2013).

[75] P. Hilaire, L. Vidro, H. S. Eisenberg, and S. E. Economou, Near-deterministic hybrid generation of arbitrary photonic graph states using a single quantum emitter and linear optics, Quantum **7,** 992 (2023).

[76] R. Stassi, M. Cirio, and F. Nori, Scalable quantum computer with superconducting circuits in the ultrastrong coupling regime, npj Quantum Inf. **6,** 67 (2020).

[77] S. Hazra, A. Bhattacharjee, M. Chand, K. V. Salunkhe, S. Gopalakrishnan, M. P. Patankar, and R. Vijay, Ring-resonator-based coupling architecture for enhanced connectivity in a superconducting multiqubit network, Phys. Rev. Appl. **16,** 024018 (2021).

[78] P. A. Spring, S. Cao, T. Tsunoda, G. Campanaro, S. Fasciati, J. Wills, M. Bakr, V. Chidambaram, B. Shteynas, L. Carpenter, P. Gow, J. Gates, B. Vlastakis, and P. J. Leek, High coherence and low cross-talk in a tileable 3D integrated superconducting circuit architecture, Sci. Adv. **8,** eabl6698 (2022).

[79] J. Johansson, P. Nation, and F. Nori, QuTiP 2: A Python framework for the dynamics of open quantum systems, Comput. Phys. Commun. **184,** 1234 (2013).

[80] T. Asano, Y. Ochi, Y. Takahashi, K. Kishimoto, and S. Noda, Photonic crystal nanocavity with a Q factor exceeding eleven million, Opt. Express **25,** 1769 (2017).

[81] H. Ren, M. H. Matheny, G. S. MacCabe, J. Luo, H. Pfeifer, M. Mirhosseini, and O. Painter, Two-dimensional optomechanical crystal cavity with high quantum cooperativity, Nat. Commun. **11,** 3373 (2020).

[82] S. M. Meenehan, J. D. Cohen, G. S. MacCabe, F. Marsili, M. D. Shaw, and O. Painter, Pulsed excitation dynamics of an optomechanical crystal resonator near its quantum ground state of motion, Phys. Rev. X **5,** 041002 (2015).

[83] M. Varnava, D. E. Browne, and T. Rudolph, Loss tolerance in one-way quantum computation via counterfactual error correction, Phys. Rev. Lett. **97,** 120501 (2006).

[84] N. Nickerson and H. Bombín, Measurement based fault tolerance beyond foliation, ArXiv:1810.09621.

[85] H. Bombín, C. Dawson, N. Nickerson, M. Pant, and J. Sullivan, Increasing error tolerance in quantum computers with dynamic bias arrangement, ArXiv:2303.16122.

[86] K. Alexander, *et al.*, A manufacturable platform for photonic quantum computing, ArXiv:2404.17570.

[87] R. Benevides, M. Drimmer, G. Bisson, F. Adinolfi, U. von Lüpke, H. M. Doeleman, G. Catelani, and Y. Chu, Quasiparticle dynamics in a superconducting qubit irradiated by a localized infrared source, Phys. Rev. Lett. **133,** 060602 (2024).

[88] M. McEwen, *et al.*, Resisting high-energy impact events through gap engineering in superconducting qubit arrays, ArXiv:2402.15644.

[89] T. Rudolph, Why I am optimistic about the silicon-photonic route to quantum computing, APL Photonics **2,** 030901 (2017).

[90] D. Bonneau, G. J. Mendoza, J. L. O'Brien, and M. G. Thompson, Effect of loss on multiplexed single-photon sources, New J. Phys. **17,** 043057 (2015).

[91] J. Kolvik, P. Burger, J. Frey, and R. Van Laer, Clamped and sideband-resolved silicon optomechanical crystals, Optica **10,** 913 (2023).

[92] D. Litinski, How to compute a 256-bit elliptic curve private key with only 50 million Toffoli gates, ArXiv:2306.08585.

[93] A. Morana, C. Campanella, J. Vidalot, V. De Michele, E. Marin, I. Reghioua, A. Boukenter, Y. Ouerdane, P. Paillet, and S. Girard, Extreme radiation sensitivity of ultra-low loss pure-silica-core optical fibers at low dose levels and infrared wavelengths, Sensors **20,** 7254 (2020).

[94] S. Krinner, S. Storz, P. Kurpiers, P. Magnard, J. Heinsoo, R. Keller, J. Lütolf, C. Eichler, and A. Wallraff, Engineering cryogenic setups for 100-qubit scale superconducting circuit systems, EPJ Quantum Technol. **6,** 2 (2019).

[95] M. Aspelmeyer, T. J. Kippenberg, and F. Marquardt, Cavity optomechanics, Rev. Mod. Phys. **86,** 1391 (2014).

[96] C. W. Gardiner and M. J. Collett, Input and output in damped quantum systems: Quantum stochastic differential equations and the master equation, Phys. Rev. A **31,** 3761 (1985).

[97] A. H. Kiilerich and K. Mølmer, Input-output theory with quantum pulses, Phys. Rev. Lett. **123,** 123604 (2019).

[98] K. S. Chou, *et al.*, Demonstrating a superconducting dual-rail cavity qubit with erasure-detected logical measurements, ArXiv:2307.03169.

[99] H. J. Briegel, D. E. Browne, W. Dür, R. Raussendorf, and M. Van Den Nest, Measurement-based quantum computation, Nat. Phys. **5,** 19 (2009).

[100] R. Riedinger, A. Wallucks, I. Marinković, C. Löschnauer, M. Aspelmeyer, S. Hong, and S. Gröblacher, Remote quantum entanglement between two micromechanical oscillators, Nature **556,** 473 (2018).

[101] L. Chen, *et al.*, Transmon qubit readout fidelity at the threshold for quantum error correction without a quantum-limited amplifier, npj Quantum Inf. **9,** 26 (2023).

[102] A. G. Fowler, M. Mariantoni, J. M. Martinis, and A. N. Cleland, Surface codes: Towards practical large-scale quantum computation, Phys. Rev. A **86,** 032324 (2012).

[103] S. Kosen, *et al.*, Building blocks of a flip-chip integrated superconducting quantum processor, Quantum Sci. Technol. **7,** 035018 (2022).

[104] A. P. M. Place, *et al.*, New material platform for superconducting transmon qubits with coherence times exceeding 0.3 ms, Nat. Commun. **12,** 1779 (2021).

[105] L. DiCarlo, J. M. Chow, J. M. Gambetta, L. S. Bishop, B. R. Johnson, D. I. Schuster, J. Majer, A. Blais, L. Frunzio, S. M. Girvin, and R. J. Schoelkopf, Demonstration of two-qubit algorithms with a superconducting quantum processor, Nature **460,** 240 (2009).

[106] F. Yan, P. Krantz, Y. Sung, M. Kjaergaard, D. L. Campbell, T. P. Orlando, S. Gustavsson, and W. D. Oliver, Tunable coupling scheme for implementing high-fidelity two-qubit gates, Phys. Rev. Appl. **10,** 054062 (2018).